Renewable Energy 206 (2023) 1020–1035

Contents lists available at ScienceDirect

Renewable Energy

journal homepage: www.elsevier.com/locate/renene

Near wake hydrodynamics and structural design of a single foil cycloidal rotor in regular waves☆

Abel Arredondo-Galeana [a,*], Gerrit Olbert [b], Weichao Shi [a], Feargal Brennan [a]

[a] Department of Naval Architecture, Ocean and Marine Engineering at the University of Strathclyde, Glasgow, UK
[b] Institute for Fluid Dynamics and Ship Theory, Hamburg University of Technology, Hamburg, Germany

ARTICLE INFO

Keywords:
Wave energy converters
Wave cycloidal rotor
Attached and vortical flow
Potential flow
Beam theory
Structural design

ABSTRACT

We present a hydrodynamic and structural model to design a single foil wave cycloidal rotor in regular waves. The hydrodynamic part considers potential flow and represents the foil as a point vortex. Unsteady effects are accounted for through Theodorsen's function. The structural part utilises beam theory to compute the bending moments and stresses on the foil of the cyclorotor. The validity of the hydrodynamic model is explored with the aid of CFD, and the CFD results are bench marked versus experimental measurements. Results show that the hydrodynamic model estimates the mean radial loading on the foil within 20%–25% in attached flow conditions, whilst it is accurate to predict the mean tangential loading only when operating close to stall, at maximum lift conditions. Because the optimal structural operation of the rotor is in attached flow conditions, and close to stall, we utilise the coupled model to design a rotor that operates optimally for a range of different sea conditions. We find that with careful dimensioning of the radius and span, power extraction in regular waves can be optimised, whilst the structural penalty is kept constant at the allowable stress level.

1. Introduction

Wave cycloidal rotors are a novel type of wave energy converter (WEC) that have gained a rejuvenated level of attention over the past years [1–6]. Although the pioneering idea of extracting wave energy through the rotational motion of a submerged foil and the use of lift forces dates back to the early 90s [7,8], recent efforts of the Atargis group in America and the LiftWEC consortium in Europe, have brought this technology closer to commercialisation.

The concept of a wave cycloidal rotor consists of a foil that rotates under a wave. The span of the foil is oriented parallel to the crest of the wave, and through rotational motion, the foil interacts with the wave particle velocity to produce lift and drag forces. Provided that the lift to drag ratio is high, the tangential component of the lift force drives the rotation of the foil and energy is extracted.

This type of WECs are classified as lift based wave energy converters [9,10]. Because their operation is based on lift forces, the hydrodynamic and structural challenges encountered in the marine environment are unique, but can also draw inspiration on other type of lift based energy devices. In contrast, for example, to vertical axis wind turbines (VAWTs), the operation of a wave cycloidal rotors in attached or separated flow is not fully understood. However, it is expected that similarly to VAWTs, the type of flow regime will have a significant effect on the hydrodynamic and structural performance of the rotor. Furthermore, the structural reliability of the foils is a critical aspect to reach a commercial stage. In particular, the unsteady loading on the foils impose large bending stresses that can cause premature mechanical failure.

Therefore, it is important to develop analytical tools that can assist in the design of this type of WECs, and that use physics informed observations to provide robustness in the design methodologies. To this date, analytical models that study wave cycloidal rotors have almost exclusively been used to assess wave radiation downstream of the device [1,2,11] and have not had a widespread use to assess structural loading. Additionally, to the best knowledge of the authors of this paper, no physics informed based approach is available in the literature of wave cycloidal rotors. Therefore, in this paper, we address these research gaps and develop an analytical model to assess structural loading on a single foil rotor, and utilise a physics informed approach to explore the flow regime where the analytical model is valid.

☆ This document is the results of the research project funded by the European Union's Horizon 2020 Research and Innovation Programme under Grant Agreement No 851885.

* Corresponding author.
E-mail addresses: abel.arredondo-galeana@strath.ac.uk (A. Arredondo-Galeana), gerrit.olbert@tu-hamburg.de (G. Olbert), weichao.shi@strath.ac.uk (W. Shi), feargal.brennan@strath.ac.uk (F. Brennan).

https://doi.org/10.1016/j.renene.2023.02.068
Received 30 September 2022; Received in revised form 3 February 2023; Accepted 15 February 2023
Available online 21 February 2023

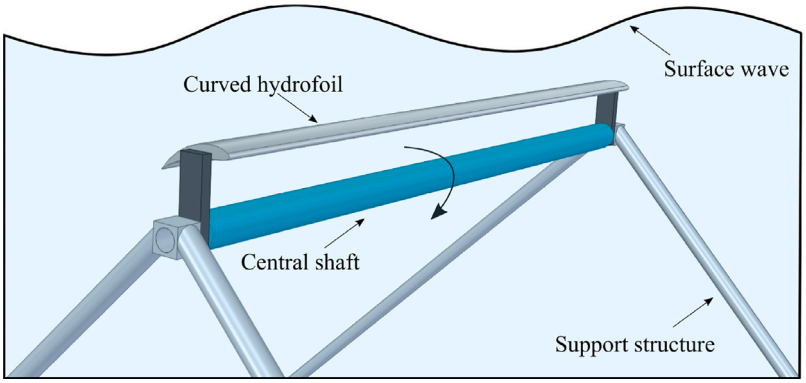

Fig. 1. LiftWEC wave bladed cyclorotor in operation near water surface and supported by two triangular frames.

Concretely, we study a single foil wave cycloidal rotor operating in two flow regimes: attached and vortical flow conditions. We assess the structural implications that these two flow regimes have in the loading of the foil. The use of an analytical model, which accounts for unsteady wake effects, is assessed in these two flow regimes to predict forces on the foil. Subsequently, we utilise the analytical model to provide structural design guidelines for large scale wave cyclorotors to chose the operational phase and radius of the rotor that optimise power extraction, and also, the span of the foil that allows the bending stresses to remain below the allowable stress level.

The work presented in this paper is a first attempt in the literature of wave cycloidal rotors to deploy a physics informed based approach to evaluate the range of applicability of a low order potential flow model, in order to design the cyclorotor with a hydrodynamic and structural balanced approach.

2. Principle of operation

In this section we present the concept of the single foil wave cyclorotor used in this study. The rotor is shown in Fig. 1. It has a curved hydrofoil connected to a central shaft. The central shaft rotates due to the motion of the foil. The shaft is held by bearings that are embedded in triangular frames. These frames act as the support structure and are fixed to the seabed. The rotor operates in close proximity to the free surface but the foil remains submerged during operation.

The hydrofoil has a uniform cross section along the span s and rotates following the wave orbital motion. The phase of the rotation is modulated so that it is different to that of the wave. This phase difference generates an inflow velocity w at an angle of attack α and hence a lift force in the hydrofoil. Provided that α does not exceed the stall angle of the hydrofoil (α_s), then the lift to drag ratio remains high and the tangential component of the lift force sustains the rotation of the foil.

The wave cyclorotor of this study is conceptually designed to operate in the Atlantic coast of France. According to Sierra et al. [12], the range of mean energy periods T_e and wave heights H_s in this region over a range of 41 years (1958–1999) lies within 8 to 10 s and 1 to 2 m, respectively. We compare these ranges to the values shown in the wave scatter plot of Fig. 2. The figure shows the data corresponding to a point in the North Atlantic at the coast of France, located at 47.84° N, 4.83° W. The figure shows T_p along the horizontal axis and H_s along the vertical axis. The data is available from the Ifremer FTP server and contains directional spectral wave data for 10 years between 2000 and 2010 [13]. In the figure, the dominant T_p lies within 6 to 10 s, and the dominant H_s lies within 1 to 2 m. Therefore, the Ifremer database is in agreement with the observations from Sierra et al. [12]. Because the Ifremer database has the data available as wave energy T_e and we use T_p in our hydrodynamic computations, we covert T_e values to T_p values through $T_e = \alpha T_p$, where $\alpha = 0.9$ for a JONSWAP wave spectrum [14].

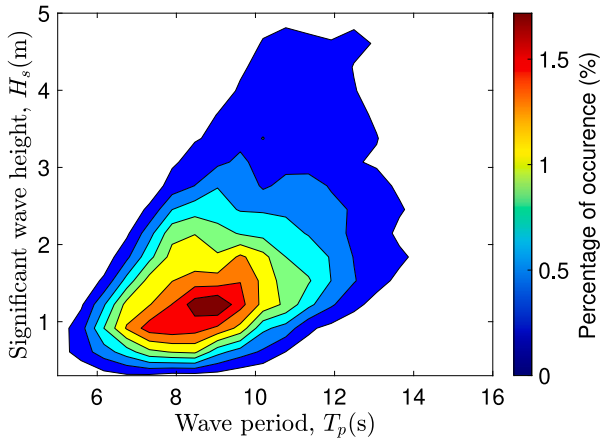

Fig. 2. Scatter plot showing energy period T_p versus significant wave height H_s of seasonal data of a point in the North Atlantic at the coast of France, located at 47.84° N, 4.83° W.

From Fig. 2, we select the wave design conditions to be a point in the region where the highest counts are found. As such, the selected wave design conditions are $T_p = 9$ s and $H_s = 1.2$ m.

3. Hydrodynamic model

We consider the single foil wave cycloidal rotor that was introduced in the previous section and we show its side view in Fig. 3. The figure shows the single foil rotor at the normalised time period $t/T_p = 0$ and at the azimuthal position $\theta = 0°$. The wave direction is from left to right and the wave particle motion is clockwise [15]. Hence, the rotation of the foil is clockwise as well. The rotor has a radius r and a submergence depth z_0 measured from the mean sea level to the central shaft. The phase angle between the foil motion induced velocity $-\mathbf{u}$ and the wave velocity component $\mathbf{v}$ is ϕ. We refer to this phase angle as the operational phase. The relative velocity and the angle of attack on the foil are $\mathbf{w}$ and α, respectively. The force components acting on the foil are lift (L) and drag (D), which can be decomposed into the radial (R) and tangential (T) force components through α.

Considering a large span hydrofoil with uniform cross section, we can assume two dimensional flow. The foil is modelled as a single point vortex moving under the free surface. As such, we describe hydrodynamic model in the following paragraphs.

Point vortex model

The complex potential of a free vortex under a free surface was derived by Wehausen and Laitone [16]. This representation has been used in the literature of wave cyclorotors to model the foils as single

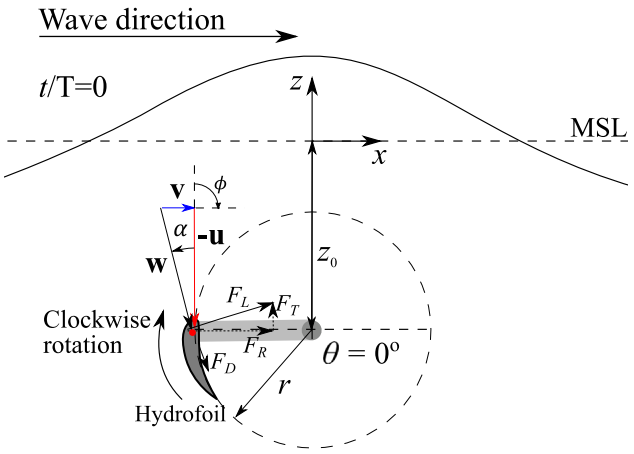

Fig. 3. Side view of a single foil wave cycloidal rotor showing the lift and drag forces (L, D) on the hydrofoil, the wave velocity v, the velocity due to the rotation of the hydrofoils $-u$, the relative velocity w and the operational phase ϕ at $t/T = 0$.

vortices [1,7,11] or to discretise the foils into multiple lump vortices [1, 11]. Here, we utilise the single point vortex representation developed by Ermakov and Ringwood [11] for a two foil cyclorotor, but adapt the model to a single foil rotor. In this paper, we consider unsteady wake effects through Theodorsen's theory.

Noteworthy, single point vortex methods have been predominantly used to predict surface elevation due to a foil near a free surface but have not been widely used to predict the loading of foils of a cyclorotor. For this reason, in this work, we will compare the single point vortex method results to numerical results obtained with the aid of CFD RANS simulations. This will enable us to assess the validity and limitations of the single point vortex model.

Concretely, the complex potential of a point vortex under a free surface [16] is given by

$$F(p,t) = \frac{\Gamma(t)}{2\pi i}\mathrm{Log}\left[\frac{p-\zeta(t)}{p-\zeta'(t)}\right] + \frac{g}{\pi i}\int_0^t\int_0^\infty \frac{\Gamma(\tau)}{\sqrt{gk}} e^{-ik(p-\zeta'(\tau))} \times \sin\left[\sqrt{gk}(t-\tau)\right] dk d\tau, \tag{1}$$

where $\Gamma(t)$ in the first term of Equation (1) is the instantaneous circulation of the point vortex that represents the foil, and $\Gamma(\tau)$ in the second term is the circulation of the point vortices at previous instants in time along the foil path, p is a point in the complex plane denoted by $p = x+iz$, $\zeta(t)$ is the position of $\Gamma(t)$ and is defined as $\zeta(t) = x_\Gamma + iz_\Gamma$, $\zeta'(t)$ is the complex conjugate of $\zeta(t)$ and denotes a mirror point vortex that imposes the impermeability condition on the free surface, such that $\zeta(t)' = x_\Gamma - iz_\Gamma$, g is the gravitational constant, k is the wave number, t is time, τ is a time parameter used to describe the time delayed influence of circulation $\Gamma(\tau)$ on the velocity field at point p and $\zeta'(\tau)$ is complex conjugate of $\zeta(\tau)$, where $\zeta(\tau)$ is the position of the point vortex at time τ.

Eq. (1) can be simplified by solving analytically the integral over k of the second term with the Dawson's function. As such, Ermakov and Ringwood [11] propose the following expression:

$$F(p,t) = \frac{\Gamma(t)}{2\pi i}\mathrm{Log}\left[\frac{p-\zeta(t)}{p-\zeta'(t)}\right] - \frac{2i\sqrt{g}}{\pi}\int_0^t \frac{\Gamma(\tau)}{\sqrt{i(p-\zeta'(\tau))}} D\left[\frac{\sqrt{g}(t-\tau)}{2\sqrt{i(p-\zeta'(\tau))}}\right] d\tau. \tag{2}$$

By taking the derivative of Equation (2), we obtain the complex velocity induced by a point vortex of circulation $\Gamma(t)$ at point p, such that

$$\frac{\partial F(p,t)}{\partial p} = \mathbf{q} = u_1 - iv_1 + u_2 - iv_2, \tag{3}$$

where the indices 1 and 2 correspond to the first and second term of Equation (2), respectively. In Eq. (3), u_1 and v_1 represent the induced velocity components of the point vortex of circulation $\Gamma(t)$ located at $\zeta(t)$ at point p. In contrast, u_2 and v_2 represent the velocity components induced by the time delayed effect of circulations $\Gamma(\tau)$ at point p, accumulated over the interval $\tau = t - T$ to $\tau = t$, where T is one cycle of rotation of the cyclorotor and is considered to be the relevant time period over which previous instances of circulation affect foil forces as observed in our CFD simulations. The time discretisation criterion was defined by $T/\Delta t = 100$, after convergence was reached in mean power values. Note that this discretisation step is higher than $T/\Delta t = 36$, previously used in [17]. Hence, the time resolution used in this study is robust and makes use of the progress in computational power over the past decade.

The explicit terms of Equation (3) are included in Ermakov and Ringwood [18] for a two foil rotor. Here, because we consider a single foil rotor, p and ζ are the same, i.e. the point at which we evaluate the influence of $\Gamma(t)$ is the same point where $\Gamma(t)$ is located. As such, only the terms related to the flow memory effect (u_2 and v_2) are considered. We note that u_2 and v_2, account for the unsteady effect that the deformation of the free surface due to previous instances of circulation and the corresponding declining response of the free surface impose in the near flow field.

Although the circulation of the foil Γ is time dependent, previous studies have considered constant Γ by keeping the angle of attack constant by adjusting the pitch angle throughout the rotation of the foil [1,2]. In this study, Γ is updated at each time step, assuming the Kutta condition, i.e. $\Gamma = L/(\rho|\mathbf{w}|)$. Although this assumption does not account for the fact that the flow around the foil is unsteady, we account for the effects of the wake in Γ by considering Theodorsen's function. Theodorsen's function accounts for the effect of a planar wake vortex sheet in the bound circulation of a foil, and in fact, it has been shown that Theodorsen's theory is resilient even in flow fields that contain nonplanar wakes and large leading-edge flow separation. This is because a trailing-edge Kutta condition can still be valid in unsteady flow fields [19]. As such, we also assume a Kutta condition at the trailing edge and the Kutta circulation around the foil. The implementation of Theodorsen's function is explained at the end of this Section.

Once $\mathbf{q}$ from Equation (3) is determined, we consider also the influence of the velocity components due to the wave and the rotation of the rotor. Fig. 3 shows that in a simplified form, the relative velocity on the foil $\mathbf{w}$ is given by the velocity triangle formed between the wave velocity component $\mathbf{v}$ and the velocity due to the rotation of the rotor $-\mathbf{u}$. By considering also $\mathbf{q}$, then the relative velocity on the foil can be defined as

$$\mathbf{w} = \mathbf{v} - \mathbf{u} + \mathbf{q}. \tag{4}$$

To compute $\mathbf{u}$, let us consider the rotor of radius r from Fig. 3. The position of the point vortex that represent the foil is given by

$$x = -r\cos(\theta(t)) \tag{5}$$

and

$$z = z_0 + r\sin(\theta(t)), \tag{6}$$

where z_0 is the submergence of the rotor, $\theta(t)$ is the angular position measured with respect to the negative horizontal axis and positive clockwise. The horizontal and vertical velocity components of the point vortex (u_x, u_z) are

$$u_x = \omega r\sin(\theta(t)) \tag{7}$$

and

$$u_z = \omega r\cos(\theta(t)), \tag{8}$$

where ω is the rotational frequency of the rotor. Note that the induced velocity due to the rotation of the point vortex is $-\mathbf{u}$, therefore we consider $-u_x$ and $-u_z$.

The wave velocity $\mathbf{v}$ and its horizontal and vertical components (v_x, v_z) are determined assuming deep water linear wave equations [20], such that

$$v_x = \frac{\pi H}{T} e^{kz} \cos(kx - \omega t) \tag{9}$$

and

$$v_z = \frac{\pi H}{T} e^{kz} \sin(kx - \omega t), \tag{10}$$

where H is the wave height, T is the wave period, k is the wave number, x and z denote the position of the hydrofoil, as defined by Eqs. (5) and (6), respectively. In the numerical computations, the wave number k is computed with the dispersion relationship [21].

The angle of attack (α) is defined as the angle between the relative velocity $\mathbf{w}$ and the rotational velocity of the rotor $\mathbf{u}$. As such, α is given by

$$\alpha = \sin^{-1}\left[\frac{||\mathbf{w} \times -\mathbf{u}||}{||\mathbf{w}||||-\mathbf{u}||}\right], \tag{11}$$

in agreement with the diagram of Fig. 1.

We define positive α anticlockwise as depicted in Fig. 3. The lift and drag force on the foil are

$$L = \frac{1}{2} C_L \rho c s |\mathbf{w}|^2 \tag{12}$$

and

$$D = \frac{1}{2} C_D \rho c s |\mathbf{w}|^2, \tag{13}$$

respectively, where C_L is the lift coefficient, C_D is the drag coefficient, ρ is the fluid density, c is the chord length of the foil, s is the span and $|\mathbf{w}|$ is magnitude of the relative velocity on the foil. The tangential force on the hydrofoil is defined as

$$T = L \sin\alpha - D \cos\alpha \tag{14}$$

and the radial force is

$$R = L \cos\alpha + D \sin\alpha. \tag{15}$$

Because T is dependent on the angular position of the point vortex (θ), the average tangential force $\overline{T}$ is expressed as:

$$\overline{T} = \frac{1}{2\pi} \int_0^{2\pi} T(\theta) d\theta. \tag{16}$$

The total mean torque ($\overline{Q}$) is

$$\overline{Q} = r\overline{T}, \tag{17}$$

and finally, the mean power output is

$$\overline{P} = \overline{Q}\omega. \tag{18}$$

Power losses due to drag

This section highlights the considerations assumed to account for power losses due to drag. Namely, we consider viscous drag and induced drag. Once the angle of attack of the hydrofoil is estimated with Eq. (11), the hydrodynamic model uses a look up table with two dimensional lift and drag coefficients, C_L and C_D, respectively, of a NACA 0015 foil section from Sheldahl and Klimas [22]. The coefficients are interpolated to account for effects of Reynolds number. As such, the drag force on the hydrofoil is computed with Eq. (13) and viscous losses are accounted for in the computation of power given by Eq. (18).

For finite aspect ratio hydrofoils, we consider also the effect of induced drag, such that

$$C_{Di} = \frac{C_L^2}{\pi \mathcal{AR}}, \tag{19}$$

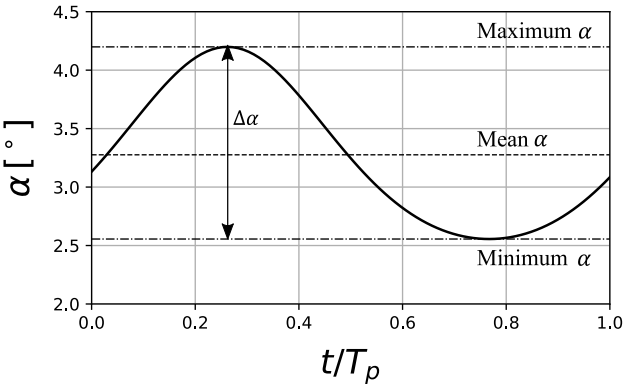

Fig. 4. Angle of attack oscillations (α) in hydrofoil 1 for one period of revolution at design sea state conditions. The parameters used to compute α are r = 5 m, c = 5 m, z_0 = 8.1 m and $\phi = 90°$.

where $\mathcal{AR}$ is the aspect ratio of the hydrofoil. The total drag coefficient is estimated such that

$$C_{D,t} = C_D + C_{D,i}, \tag{20}$$

where C_D is drag of an infinite span hydrofoil.

Angle of attack oscillations (α)

In Fig. 4, we present the angle of attack oscillations (α) throughout one period of revolution at $\phi = 90°$ for the single foil of the cyclorotor, as predicted by the single point vortex model. For the simulation of Fig. 4, we use a monochromatic wave with wave height $H = H_s/\sqrt{2}$, where H_s represents the wave height of the fundamental wave from the panchromatic spectrum at wave design conditions, i.e. H_s = 1.2 m. We assume the same wave period T for the monochromatic wave to that of the fundamental wave of the panchromatic wave spectrum at wave design conditions, i.e. $T = T_p$ = 9 s. The rotor parameters are set to r = 5 m, c = 5 m, z_0 = 8.1 m and ϕ = 90°. To illustrate periodic oscillations in Fig. 4, we do not include the term $\mathbf{q}$ to compute $\mathbf{w}$ and α from Eqs. (4) and (11), respectively.

It can be seen, that the maximum angle of attack oscillation occurs when the foil is closest to the water surface. Furthermore, the oscillations are asymmetric, i.e. they deviate more from the mean α in the first half of the cycle and less in the second half. This is reminiscent of the oscillations that occur in cross flow turbines [23,24]. Although in the example of Fig. 4, the amplitude of α is not severe, it is likely that under different wave conditions the oscillations of α increase and dynamic stall – the ability of a rotor to maintain lift through severe angles of attack and in the presence of vortex shedding [25] – occurs. In Fig. 4, the maximum, minimum and mean values of α are highlighted with dotted lines, whilst the peak to peak amplitude is denoted as $\Delta\alpha$.

Hence, because dynamic stall is not accounted for in the single point vortex model, a case where the flow remains attached and a case where dynamic stall is likely to occur will be investigated in this paper with CFD simulations. This with the aim to assess the validity of the point vortex model in different scenarios. This type of assessment has not been carried out in the literature of wave cycloidal rotors. As a second novel contribution of this work, we model wake effects through Theodorsen's function. This correction is explained in the following section.

Unsteady flow

The effect of the wake vorticity in the strength of the bound circulation of the foil is accounted for with Theodorsen's function $C(k)$. The function serves to introduce an amplitude reduction and phase lag on the circulatory part of the lift response [26]. Although originally developed for small angle of attack oscillations, Theodorsen's theory

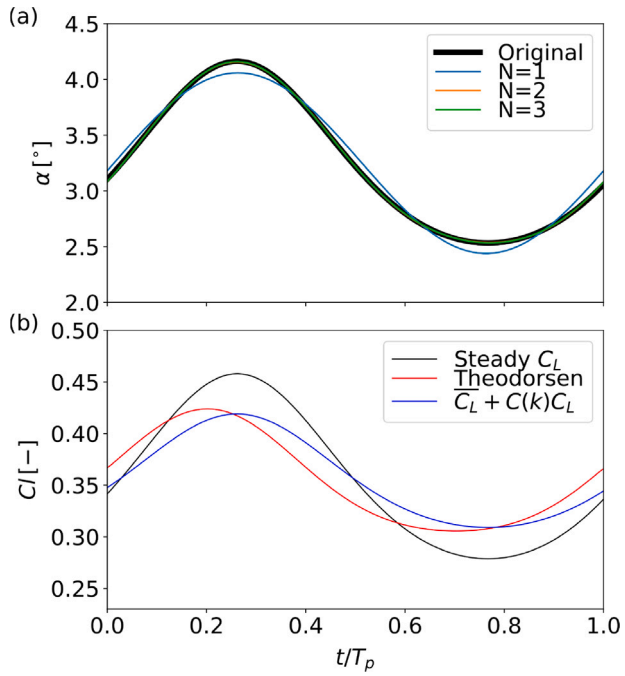

Fig. 5. (a) Oscillations of α approximated with 3 Fourier harmonics and (b) steady lift coefficient (C_L) and unsteady $C_{L,u}$ using Theodorsen's function to consider wake effects.

has been demonstrated to work satisfactorily for large angle of attack oscillations in a wide range of kinematics that include pitching, heaving or a combination of these maneuvers [19,27,28]. Here, we consider the formulation of the unsteady lift coefficient ($C_{L,u}$) for pure angle of attack oscillations, such that

$$C_{L,u} = 2\pi C(k)\alpha + \frac{\pi c\dot{\alpha}}{2|\mathbf{w}|}, \tag{21}$$

where $C(k)$ is Theodorsen's function, k is the reduced frequency, α and $\dot{\alpha}$ are the angle and rate of change of the angle of attack, respectively, and $|\mathbf{w}|$ is the magnitude of the freestream velocity. The first term, on the right hand side of Eq. (21), is the circulatory component of the lift coefficient. The second term is the added mass contribution.

Theodorsen's function is only applicable for sinusoidal oscillations. Hence, here, because the oscillations of α are non sinusoidal, we follow the procedure proposed by Ōtomo et al. [27]. We approximate the oscillations of α for a full cycle of rotation in the cyclorotor through the first ten Fourier harmonics. Note that for clarity of the figure, Fig. 5a shows only three harmonics denoted by $N = 1..3$. The corrected lift coefficient is computed for each harmonic and the total lift coefficient is computed by adding the lift coefficient of all of the harmonics. As an example, the lift coefficient computed with the steady lift coefficient and Theodorsen's theory are shown in Fig. 5b in black and red, respectively.

In Fig. 5b, two main effects are noted in the red curve, due to the effect of the wake, with respect to the black line that denotes the steady C_L. The first effect is that the peak to peak value decreases with the unsteady correction. The mean value of the unsteady lift, however, is similar to the one of the steady case. The second noteworthy effect is that there is a lag introduced to the lift response in the unsteady response (red curve).

For low Reynolds numbers, we find that Theodorsen's model over-predicts the lift response because the viscous effects contained in the lift coefficient table from Sheldahl and Klimas [22] is lost. This is because the first term of Eq. (21) considers a lift curve slope of 2π that grows with α. Hence, we approximate the circulatory term by adding the mean value of the steady lift coefficient ($\overline{C_L}$) to the fluctuations of C_L, mitigated by Theodorsen's function, such that $C_{L,u} \approx \overline{C_L} + C(k)C_L$. This is represented by the blue curve in Fig. 5b.

Note that in this paper, we use the mean values computed with the single point vortex model, corrected with Theodorsen's function, for structural design purposes. However, because we use mean force values, the lack of wake effect modelling would not be detrimental in our design estimations. This is because the difference between the mean steady and unsteady C_L is not significant, as it is shown in Fig. 5b.

4. CFD model

The point vortex method applied in this work represents a numerically efficient approach to design wave cycloidal rotors. However, the consideration of a number of effects in cyclorotor hydrodynamics such as surface drag, wake vorticity and flow separation is of empirical nature. In order to obtain an understanding of the reliability of the point vortex method in design of the cyclorotor, we conducted CFD numerical simulations.

The simulation of wave energy converters in CFD based numerical wave tanks allows the advantage that aperiodic, non linear and viscous effects are inherently considered. With increasing availability of computational resources, these methods have increased in popularity for the investigation of specific hydrodynamic effects of wave energy converters [29]. As such, the numerical model employed in the presented work corresponds to the setup described and validated in [30].

The fundamental equations which form the basis of the CFD model are the Navier Stokes and the continuity equation, such that

$$\rho\frac{\delta u}{\delta t} + \rho\mathbf{u}\cdot\nabla\mathbf{u} = -\Delta p + T + \rho\mathbf{f_b} \tag{22}$$

$$\nabla\cdot\mathbf{u} = 0, \tag{23}$$

respectively. In Eq. (22), the two terms on the left hand side represent the local and the convective acceleration, respectively, and ∇ is the del operator and $\mathbf{u}$ is the velocity vector. On the right hand side of Eq. (22), $-\Delta p$ is the pressure gradient, T is the viscous term and $\rho\mathbf{f_b}$ represents the body force. The formulations shown in Eqs. (22) and (23) assume the fluid as incompressible, and they describe the conservation of momentum and mass in the fluid, respectively.

The solution of the equations is achieved by employing a finite volume based approach. The numerical domain is discretised by a finite number of cells and the equations are solved for pressure and velocity in each cell. As described in [30], the Reynolds averaged form of the Navier Stokes equation (RANS) can be employed for modelling of the cyclorotor, as it allows to significantly reduce the computational time compared to methods considering all turbulent time scales such as Detached Eddy Simulations (DES) or Large Eddy Simulations (LES). Turbulence modelling is performed through a modified version of the $k\omega SST$-model originally presented in [31]. The model is extended by the turbulence limiters proposed in [32,33] to prevent an overproduction of turbulence in the vicinity of the free surface and near the stagnation points of the foil. The $k\omega SST$-model has been shown to deliver good performance for unsteady foil motion when employed with adequate mesh structure and resolution [34,35]. In fact, RANS models have been shown to model separation satisfactorily when separation occurs at the leading edge [36]. When applied in cyclorotor simulations, the model has been shown to perform equal to or better than other eddy viscosity models [37,38]. While the model is not as reliable as DES or LES methods in predicting mid-chord separation, reattachment and wake recovery (see e.g. [39]), the required increase in grid and time resolution as well as the three-dimensionality requirement [38] increase simulation times by orders of magnitude, which is considered unjustifiable at the current stage.

The multi phase flow problem is treated using a Volume of Fluid (VoF) approach [40]. The two phases (air and water) are treated as immiscible, while local flow properties such as density or viscosity are

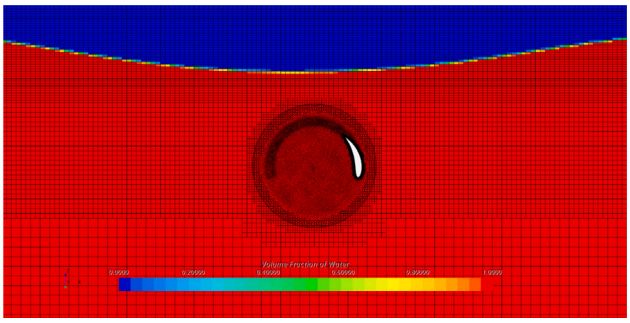

Fig. 6. Volume fraction and grid resolution in CFD-simulation of single foil rotor in regular wave.

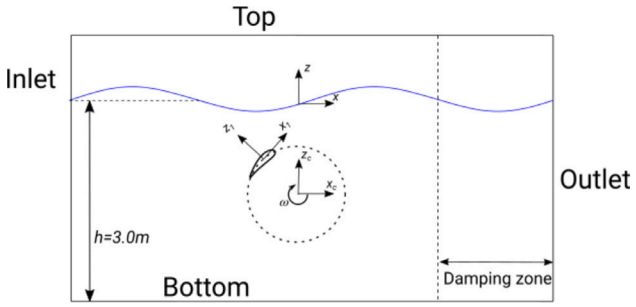

Fig. 7. Domain setup employed in CFD simulations with inlet, outlet, top and bottom boundaries, and the damping zone.

approximated as cell averaged values using the volume fraction γ. This variable indicates to which degree a cells is filled with water (1 meaning only water in cell) and is treated numerically with a transport equation in analogy with Eq. (23).

In all simulations presented in this study, the free surface interface is resolved with 120 cells per wavelength and 15 cells per wave height. Stepwise coarsening of the mesh structure away from the free surface is applied as proposed in [41]. A section of the mesh in the vicinity of rotor and free surface is shown in Fig. 6.

The numerical domain is split into two parts to model rotor motion: a background domain, which is fixed in space, and an overset domain, which rotates around the rotor axis at constant velocity. The foil geometries are embedded in the latter, resolved with 140 cells per chord length. Normal to the wall, the dimensionless wall distance is kept at $y^+ < 0.3$ due to the comparatively low Reynolds number of the investigated model scale cyclorotor. A growth factor of 1.1 is employed in all simulations. The radius of the overset domain is $1.4r$. At the interface of the domains, the solution is transferred between grids by means of interpolation (cf. e.g. [42]).

In all simulations, the background domain is defined with a total length of 8λ, with λ corresponding to the wave length of the respective simulation case approximated based on Stokes fifth order wave theory [43]. The rotor axis is located at the longitudinal centre of the domain. In the lateral direction, the domain is discretised using a single cell layer, with symmetry conditions applied on each lateral wall, thus effectively providing a two dimensional setup. At the inlet, the volume fraction and velocity of the target wave are prescribed as a Dirichlet boundary condition, using the time varying values approximated again using fifth order wave theory. A sketch of the domain is shown in Fig. 7.

The bottom of the domain is modelled as a wall. The top boundary is defined with atmospheric pressure levels. At the outlet, the hydrostatic pressure profile and volume fraction of a calm free surface are defined as a boundary condition. A damping zone extending over a length of $x_d = 2.5\lambda$ is defined upwave of the outlet boundary to prevent reflections. The damping method presented in [44] is employed for this purpose. When employing the described setup, reflection levels of approximately 1% were found in [30], following the approach described in [45]. As such, the current setup yields a minimal and satisfactory level of reflections for every tested case.

We include a grid independence study in Appendix. Note that the time step size was kept constant through all simulations, with Δt corresponding to $\Delta\theta = \frac{\sqrt{2}}{2}^{\circ}$, which was found to provide $CFL < 0.25$ in the vicinity of the free surface in all simulations. The time step size was found to provide convergence of solution in time in previous investigations of cyclorotor hydrodynamics [37,38,46].

Table 1
Mechanical properties of moderate strength offshore steel.

Property	Threshold (MPa)
Yield stress (σ_y)	350
Ultimate strength (σ_u)	410
Allowable stress (σ_a)	117

5. Structural model

We select a moderate strength steel for offshore applications [47], as the construction material for the foil. The mechanical properties of this type of steel are listed in Table 1. In the table, the allowable stress level is defined as one third of the yield stress level (σ_y). However, different thresholds can be selected according to design requirements.

The hydrofoil cross section is depicted in Fig. 8. The foil is a curved NACA 0015 whose camberline follows the curvature of the circumference of the cyclorotor. The chord length c is measured from leading edge to trailing edge as shown in the figure. An inner skin thickness of 10 mm is considered for the walls of the foil. This is a typical thickness that is commercially available for offshore steel plates and for hollow square sections. The trailing and leading edge structural components of the foil are fairings, while the middle section is the spar that provides the structural strength to the foil. The relevant dimensions of the spar and its centroid are highlighted in Fig. 8.

The second moment of area $I_{\hat{x}\hat{x}}$ of any given cross section can be computed as

$$I_{\hat{x}\hat{x}} = \int z_n^2 dA, \tag{24}$$

where z_n denotes the distance from the neutral axis of the section to the centre of an infinitesimal area element dA within the area delimited by the boundaries of the cross section. As an alternative method, $I_{\hat{x}\hat{x}}$ can also be determined in any state of the art CAD software. In this work, we utilise CAD software Solid Edge, version 2020, to compute $I_{\hat{x}\hat{x}}$. By varying the chord of the foil and utilising a constant thickness of 10 mm, we utilise a look up table to feed into the structural model the value of $I_{\hat{x}\hat{x}}$ for the spar cross section.

Once the total $I_{\hat{x}\hat{x}}$ has been computed for the foil, we now focus on computing the bending moments and stresses on the foil. We model the foil as a beam and consider two benchmark types of loading: (1) uniform loading and (2) elliptical loading. The first type of loading can be promoted through large spanned hydrofoils with winglets. A large span can promote two dimensional flow, whilst winglets can prevent tip losses [48]. The second type of loading is typical of elliptical planforms [48,49], as the one used in the Spitfire aircraft. This is a planform that provides a uniform lift coefficient and uniform induced angle of attack throughout its span.

The two types of loading are illustrated in Fig. 9. In the figure, the vertical axis shows the normalised distributed load, where w_{UL} and w_{EL} are the maximum amplitude of the uniform and elliptical loading, respectively. The horizontal axis shows the spanwise coordinate y, where $y = 0$ is the origin and $y = s$ is the span of the foil.

In order to obtain the bending moments and stresses that act on the beam, we obtain expressions for the distributed loading and forces that

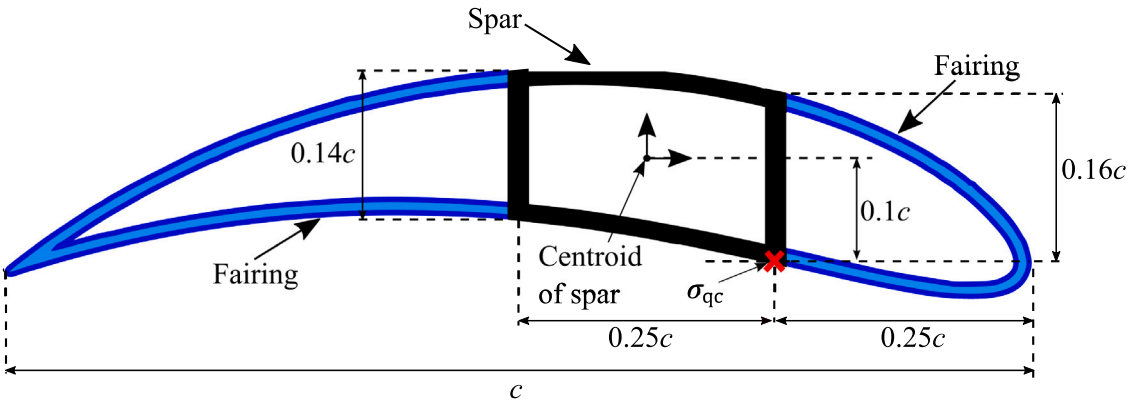

Fig. 8. (a) Curved hydrofoil cross section showing centroid and σ_{qc}. The latter is computed at the quarter chord and suction side of the foil (red marker). This point intersects the path of the radial force and needs to be structural resilient.

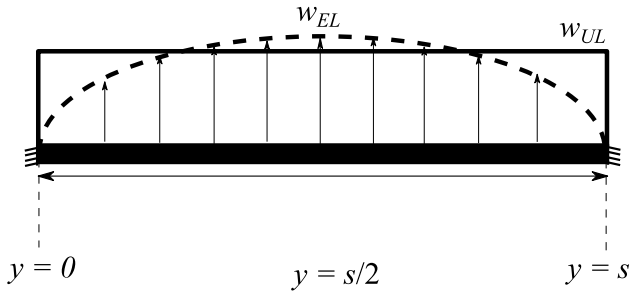

Fig. 9. Foil of cyclorotor subject to uniform and elliptical loading. The maximum distributed load is w_{UL} and w_{EL} for uniform and elliptical loading, respectively. The origin of the y-axis is defined in the figure and s is the span of the foil.

act on the beam as a function of y. We refer to these terms as w_y and F_y, respectively. For uniform loading

$$w_y = w_{UL}, \tag{25}$$

whilst for elliptical loading

$$w_y = w_{EL}\sqrt{1 - \frac{4(y - s/2)^2}{s^2}}. \tag{26}$$

The force F_y is the area under w_y. Hence, considering midspan of the foil, i.e. $y = s/2$, for uniform loading

$$F_y = w_{UL}y \tag{27}$$

and for elliptical loading

$$F_y = \frac{\pi w_{EL}y}{4}\sqrt{1 - \frac{4(y - s/2)^2}{s^2}}. \tag{28}$$

Noteworthy, for elliptical loading the area under w_y has the shape of a quarter of an ellipse with a height defined by Equation (26) and a base y, whilst for uniform loading the shape is a rectangle of height w_{UL} and base y.

Eqs. (27) and (28) are used in the static equilibrium equations of a fixed beam to solve for the shear forces V and the bending moments M. To solve for M, the centroid or point of action of F_y is determined. For a rectangular shape (uniform loading), the centroid is at the symmetry line of the rectangle. For a quarter of an ellipse, the centroid is located at $4y/3\pi$ with respect to the origin.

The static equilibrium equations yield a further unknown, which is the bending moment at the fixed end of the beam. As such, we introduce the differential equation of the elastic curve, such that

$$EI_{\hat{x}\hat{x}}\frac{d^2z}{dy^2} = M, \tag{29}$$

where E is the elastic modulus of the material, $I_{\hat{x}\hat{x}}$ is the second moment of area of the cross section, M is the bending moment and z is the deflection of the beam. Eq. (29) is integrated twice and solved for z. A set of boundary conditions are defined, the maximum deflection of the beam at $dz/dy = 0$, and the zero displacement point at $z = 0$. The maximum deflection occurs midspan of the beam, whilst zero deflection occurs at the fixed ends.

The resulting integrals are solved analytically in Mathematica and numerically with Python. Results of the uniform loading case are verified versus commercial solvers SkyCiv and ClearCalcs. The procedure described here can be applied to different types of loading provided that their spanwise distribution is known. Further examples of loading can be found for example in Taylor and Hunsaker (2020) [50].

Lastly, we compute the bending stresses at the spar of the foil, at the quarter chord position of the foil and at the suction side. We denote these stresses as σ_{qc} and denote their location in Fig. 8 with a red marker. Note that, the red marker shows a point in the foil, that is subject to large suction peaks due to the path of the radial force. Therefore, the spar requires to be structurally resilient. Hence, σ_{qc} is defined as

$$\sigma_{qc} = \frac{M_{max}z_{qc}}{I_{\hat{x}\hat{x}}}, \tag{30}$$

where M_{max} is the maximum amplitude bending moment computed at the fixed end of the beam, and z_{qc} is the vertical distance from the centroid of the foil to the location of σ_{qc}. In this case, $z_{qc} = 0.1c$, as shown in Fig. 8.

The coupling of the structural and hydrodynamic model is performed in Python. This allows for a structurally computationally inexpensive analysis and for a powerful evaluation tool that can be used to design large scale to full scale wave cycloidal energy converters. In the next section, we present the flow field around a laboratory scale cycloidal rotor to understand the effects of attached and separated flow conditions in the loading of the foil. We then assess the validity of the hydrodynamic model in these two flow regimes. In the remaining of the paper we use the coupled hydro-structural model that we introduced in Sections 3 and 5 to determine the optimum rotor radius and span to achieve a balanced hydrodynamic and structural performance in wave design conditions and at different sea states.

6. Results

6.1. Vorticity flow fields

To understand better the fluid dynamics and structural response of the single foil cyclorotor, we firstly study the flow field around a laboratory scale size rotor. The flow field is computed through two dimensional RANS simulations. The rotor radius is $r = 0.3$ m and the

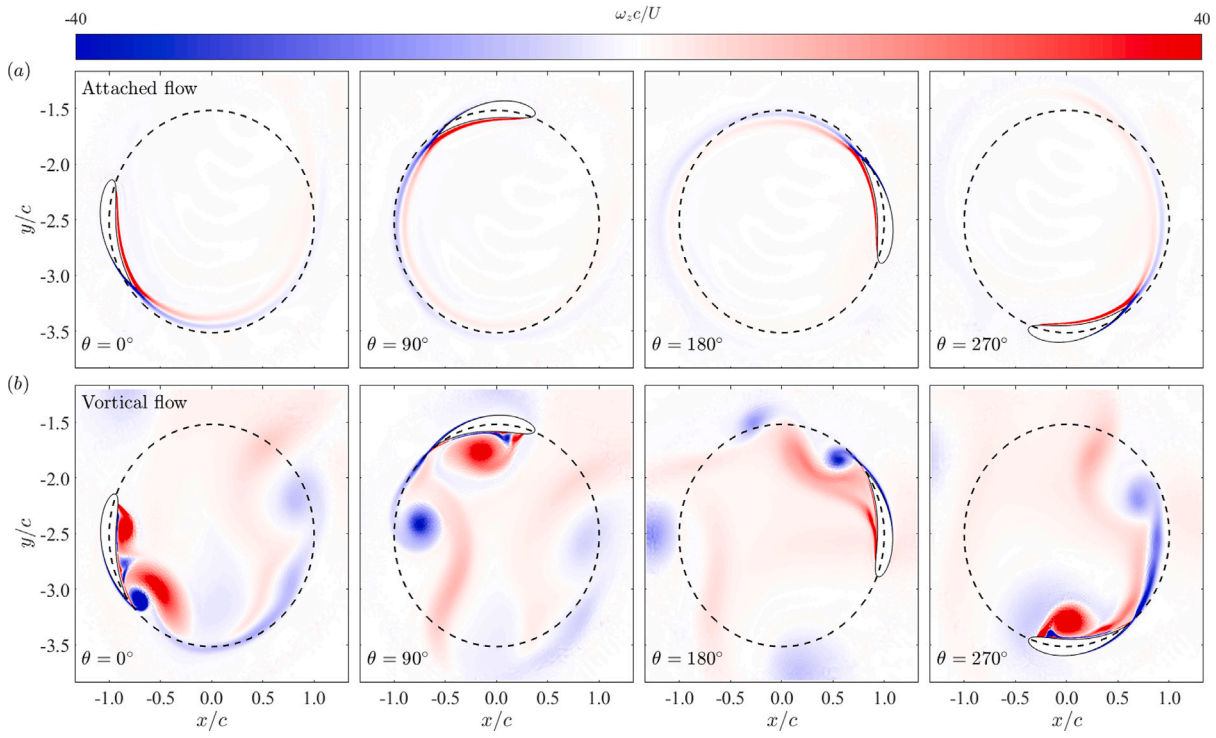

Fig. 10. Vorticity plot of single foil wave cycloidal rotor operating in (a) attached and (b) vortical flow conditions at $\theta = 0°$, 90°, 180° and 270°.

chord length of the foil is $c = 0.3$ m. The submergence of the rotor is $z_0 = -2.5c$. The foil rotates clockwise and the wave direction is from left to right. The initial position of the rotor is defined as $\theta = 0°$, with the shaft of the foil aligned to the negative horizontal axis. The operational phase ϕ is 90°, as depicted in Fig. 3.

Two monochromatic waves cases are studied. One where the flow remains attached ($T = 1.8$ s, $H = 0.253$ m) to the foil and one where the flow separates and is dominated by vortex flow ($T = 2.4$ s, $H = 0.313$ m). These two cases are chosen because of the contrasting flow features that are likely to yield different structural loads. We refer to the cases as attached and vortical flow cases, respectively. We hypothesise that the contrasting flow features between these two cases are due to the different range of α experienced by the foil. We quantify, with the point vortex model, the range of α for the two cases in Section 6.2.

Figs. 10a–d and 10e–h show the vorticity flow fields for the attached and vortical flow conditions, respectively. Four azimuthal positions are shown: $\theta = 0°, 90°, 180°$ and 270°, which are shown from left to right in the two rows of the Fig. 10. The simulations show periodic vorticity results during one cycle of rotation T after $35T$.

The attached flow case shows that the vorticity field is similar for the four azimuthal positions. Positive areas of vorticity emerge near the leading edge and are distributed along the inner side of the foil. In contrast, negative areas of vorticity are generated in the outer side of the foil, but these areas occur downstream of the mid chord. The wake of the foil follows the circumferential path of the rotor and it starts to dissipate approximately at a distance of $2.5c$ downstream of the foil. The circumferential path is denoted by a black dotted line in the figures. Noteworthy, the wake is fully dissipated at a distance of $4c$. This is approximately equivalent to a full cycle of rotation T and is the lifetime of the wake used in Section 3.

The vortical flow case shows a more dynamic flow field in the four azimuthal positions. At $\theta = 0°$, a leading edge vortex (LEV) of positive vorticity and trailing edge vortex (TEV) of negative vorticity start to emerge both from leading and trailing edge, respectively. At $\theta = 90°$, a large LEV is formed and convected along the suction side of the foil. The LEV forms a vortex pair with the coherent TEV that is located at a distance of about $1c$ downstream of the trailing edge. Subsequently, at $\theta = 180°$, the LEV has dissipated and negative vorticity is shed in the form of a starting trailing edge vortex. A new layer of positive vorticity starts to form and to detach on the inner side of the foil. Lastly, at $\theta = 270°$, the positive vorticity layer observed at $\theta = 180°$ has rolled up into a leading edge vortex, which induces a counter rotating secondary vortex of negative vorticity on the surface of the foil . At the same time, the TEV travels along the circumferential path and is found approximately at a distance of $2.5c$, and has started to dissipate.

It is noted that in the vortical flow condition, the LEVs convect along the suction side of the foil at about $t = 0.5T$ and this will possibly be reflected in the instantaneous loading of the foil. Furthermore, the suction side is the inner side of the foil throughout the full cycle of rotation. This is similar to what is typically observed in a vertical axis wind turbine under dynamic stall, where the suction side is also located at the inner side of the foil [23,51]. However, in VAWTs, the suction side remains on the inner side of the foil only for half a cycle of the rotation, whilst for the second half the suction side changes to the outer side of the foil. For a cyclorotor in regular waves, the suction side remains on the inner side during the full rotation. This is because the wave velocity component acts always normal to the outer side of the foil.

In the next section, we select the instantaneous flow field at $\theta = 90°$ as a representative case of flow, for both attached and vortical conditions to analyse the flow field around the cyclorotor in more detail.

6.2. Topology of flow

The instantaneous streamlines surrounding the foils at $\theta = 90°$ for attached and vortical flow conditions are shown in Fig. 11a and 11b, respectively. This position is selected because it is when the foil is closest to the free surface, and the one where the foil experiences the highest angle of attack and therefore the highest loading. In the figures, the streamlines highlight the dominant directions of the flow around the foil.

Fig. 11a shows that the dominant flow direction on the pressure side and upstream of the leading edge of foil is that of the wave velocity component. In these areas, the direction of the streamlines is mostly

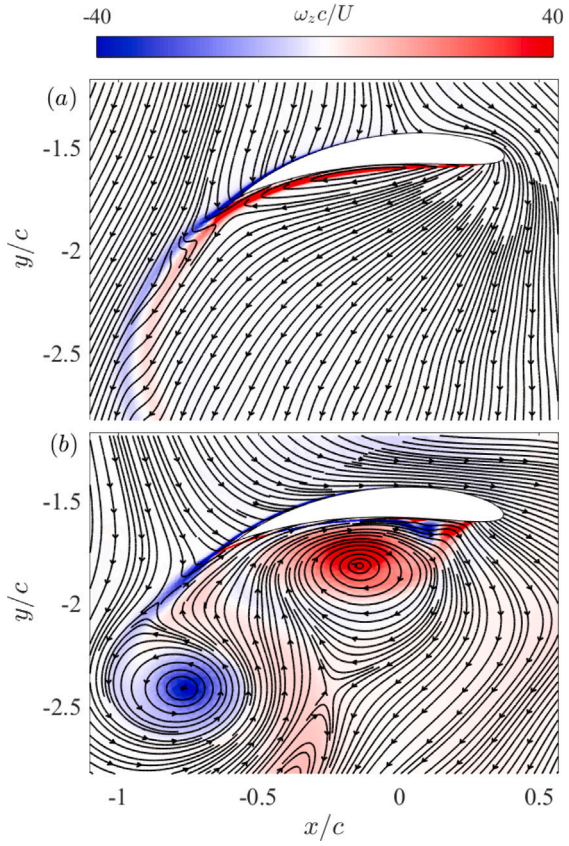

Fig. 11. Velocity fields around hydrofoil at $\theta = 90°$ for (a) attached and (b) vortical flow conditions.

downwards. We recall that the wave velocity component acts normal to the motion of the foil because $\phi = 90°$. In contrast, Fig. 11b shows that although the wave direction also points downwards, as evidenced behind the trailing edge of the foil at the upper left side of the figure, there is a strong jet of flow opposing the wave velocity component due to the vortex pair formed by the LEV and TEV. This opposite jet forces the flow on the pressure side of the foil to bend and be more tangential to the foil, as opposed to more normal, as it is in the case of Fig. 11a.

Two recirculation zones are identified in both of the figures with the streamlines. In the attached flow case of Fig. 11a, a small circulation bubble is present on the suction side of the foil. This recirculating zone is also common in steady translating flow on the concave side of curved surfaces, such as circular arcs at low Reynolds numbers [52]. A larger circulation zone with high content of positive vorticity is formed on the vortical flow case in Fig. 11b. In this case, an LEV with a diameter size of approximately $0.5c$ appears on the suction side of the foil. Contrary to the circulation zone in Fig. 11a, the LEV in Fig. 11b is mirrored by a TEV of opposite circulation. As such, according to impulse theory, the vortex pair will have an instantaneous influence in the force time stamp of the foil through growth rate of circulation ($\dot{\Gamma}$) and through the advection velocity of the LEV ($\dot{d}$) [27,53].

The average Reynolds number Re_{av}, for attached and vortical flow case, is computed by considering the average angular velocity (U_{av}) of the foil. Here, $U_{av} = (2\pi r/T)$. Hence, $R_{av} = 300{,}000$ for the attached flow case, and $R_{av} = 250{,}000$ for the vortical flow case. However, the different flow physics observed between the attached and vortical flow cases are likely to be due to the angle of attack that the foil experiences in each case, rather than due to the difference in the Reynolds number. In fact, using Eq. (11), the range of α oscillations for the attached flow case ranges between $6° < \alpha \leq 14°$, whilst for the vortical flow case, the range is $14° < \alpha \leq 21°$.

Table 2
Wave characteristics during experimental test runs of single foil rotor in monochromatic waves.

Wave/rotor period	1.6 s	1.8 s	2.0 s	2.2 s	2.4 s
Wave height	0.236 m	0.253 m	0.286 m	0.310 m	0.313 m

We estimate the error in the estimation of α with Eq. (11), by considering the stall angle α_s of a NACA 0015 at $Re = 360{,}000$ as a reference point. According to Sheldahl and Klimas [22], the stall angle for this foil at this Re is $\alpha_s = 12°$. Because in the attached flow case, the computed α oscillations exceed α_s by 2° and stall does not occur, this could mean an error in the α computation by the potential flow model of about 2°.

In the next Section, because the single point vortex model does not account for the flow physics that occur in the vortical flow case, we assess the accuracy of the point vortex model versus the CFD and experimental data, for different regular wave cases.

6.3. Point vortex model assessment

In this Section, we compare the forces computed with the point vortex model (PV) to those computed with RANS CFD simulations, and experimental two dimensional data from the LiftWEC project [54]. The tested cases are given in Table 2. Note that in Table 2, the attached and vortical flow cases correspond to $T = 1.8$ s, $H = 0.253$ m and $T = 2.4$ s, $H = 0.313$ m, respectively.

The methodology for the CFD simulations is described in Section 4, and is further developed in Olbert et al. [5,30]. The experimental data is obtained from two dimensional tests with a single foil cyclorotor device performed in the wave flume of École Centrale de Nantes [54]. In the experiments, the rotor was held by cylindrical fairings that were embedded in the walls of a 17 m long subchannel. The width of the subchannel was $1.6c$, which was the same width of the cyclorotor prototype. The subchannel provided a two dimensional set up inside of the water flume. The rotor was tested in regular waves and both the radial and tangential forces on the foil were measured with load sensors. The rotor parameters r, c, z_0 and ϕ used in experiments, CFD simulations and point vortex model are the same as those described in Section 6.1.

The resulting mean radial and tangential force coefficients ($\overline{c}_{\mathrm{rad}}$, $\overline{c}_{\mathrm{tan}}$), for the cases of Table 2, are shown in Fig. 12. The results for the CFD, point vortex model (PV) and experimental tests are plotted with black, blue and magenta markers, respectively. Note that, the experimental data is plotted with error bars representing the standard deviation. The relatively high experimental uncertainty was due to diffraction and reflection effects observed close to the subchannel mouth and exit. However, it can be seen that, the behaviour of mean radial forces is satisfactorily predicted by the CFD simulations. We note, however, that the CFD simulations, over estimate the mean tangential force coefficients at $T = 1.6$ s, $H = 0.236$ m and $T = 1.8$ s, $H = 0.253$ m. This discrepancy is attributed to physical effects, such as frictional losses and wave reflections that affected the experimental measurement, but that are not included in the CFD methodology.

Hence, the point vortex model is assessed against the CFD simulations only. Fig. 12a, shows that the radial force coefficient is predicted within 20%–25% for $T = 1.6$ s, $H = 0.236$ m; $T = 1.8$ s, $H = 0.253$ m and $T = 2.0$ s, $H = 0.286$ m. In these cases, the mean angle of attack grows from 7.4 to 12.6°, and the flow is likely to remain attached or begin slightly to separate towards 12°. At $T = 2.2$ s, $H = 0.310$ m and $T = 2.4$ s, $H = 0.313$ m, the mean radial force coefficient is predicted within 35%, and the flow is likely to be fully separated. In fact, we recall that at $T = 2.4$ s, $H = 0.313$ m, Section 6.1 shows that the flow is in fact separated.

Fig. 12b shows that the tangential force coefficient is predicted accurately, within 3%, only at $T = 1.8$ s, $H = 0.253$ m. Whilst the

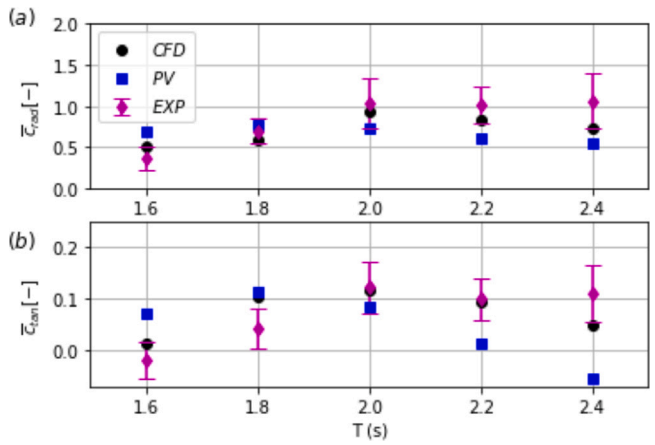

Fig. 12. CFD, point vortex model (PV) and experimental (EXP) data points showing: (a) mean radial force coefficient ($\overline{c}_{rad}$) and (b) mean tangential coefficient ($\overline{c}_{tan}$), for a single foil rotor in monochromatic waves, with the parameters shown in Table 2.

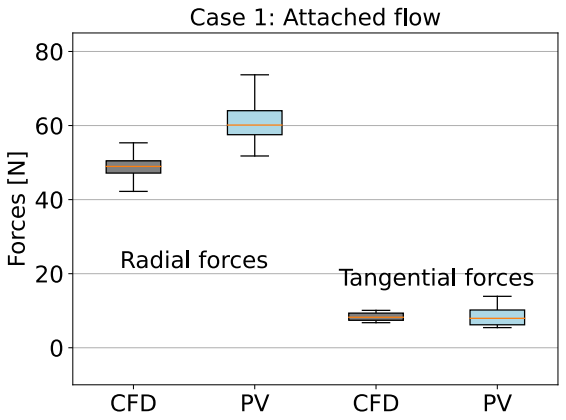

Fig. 13. Box plot diagram showing the radial and tangential forces predicted by CFD and the point vortex (PV) model for the attached flow comparison.

accuracy of the point vortex model versus CFD simulations drops at $T = 1.6$ s, $H = 0.236$ m and $T = 2.0$ s, $H = 0.286$ m. Evidently, the point vortex model fails to predict the mean tangential force coefficient at $T = 2.2$ s, $H = 0.310$ m and $T = 2.4$ s, $H = 0.313$ m. Assuming that tests $T = 1.6$ s, $T = 1.8$ s and $T = 2.0$ s have the same Re_{av}, we find that case $T = 1.8$ s, $H = 0.253$ m is the case with the highest mean lift coefficient ($\overline{C}_L = 0.78$). This occurs because the mean angle of attack is also the highest ($\overline{\alpha} = 10.1°$), but remains below the stall angle ($\alpha_s \leq 12°$). Hence, when the rotor operates at optimum conditions, close to stall, the point vortex model is a useful tool to predict the mean tangential loading on the foil.

The observed discrepancies between the point vortex model and the CFD results could be due to error in the estimation of the oscillations of the angle of attack and also, due to viscous effects around the foil that are not considered in the single point vortex model. Another possible reason for the discrepancies is that dynamic lift is generated which allows for temporary exceedance of the stall angle while keeping the flow attached. Furthermore, variance around the mean force can be due to incipient stall, which is evidenced by the recirculation bubble shown on the suction (concave) side of the foil in Fig. 11a.

However, we note that because the point vortex model predicts within 20%–25% the mean radial loading on the foil in attached flow conditions, and provides an accurate estimate of the tangential loading on the foil when the rotor operates close to stall, i.e. maximum lift conditions, we consider the point vortex model to be a useful design tool to estimate the mean forces on the foil in optimal operating conditions. Furthermore, the computational speed of the point vortex model (1 minute/case) compared to the time required to carry out one CFD simulation (24 hours/case) in a standard desktop computer, justifies the use of the point vortex model as a first design tool for cycloidal rotors. Furthermore, it allows for coupling of the structural model to allow an initial assessment of the structural design of this type of rotors. Lastly, because the rotor needs to be structurally resilient, it needs to operate in attached flow conditions. This is because in vortical flow conditions, similarly to vertical axis wind turbines [24], the variance of the forces can result in an increase in fatigue damage and therefore reduce the life of the rotor. As such, because the optimal operating conditions are those of attached flow, in Sections 6.5 and 6.6, we perform the structural design of a large scale rotor using the single point vortex model to predict mean loads on the foil, and to size the rotor radius and span.

The effect of incorporating Theodorsen's function is analysed for $T = 1.8$ s, $H = 0.253$ m, i.e. the attached flow case, with the CFD and PV results. We use whisker plots to show the force data in Fig. 13. The whisker plots show the mean value, the maximum and the minimum values of the radial and tangential forces during one cycle of rotation T after $35T$. This ensures that any transient force resulting from initial accelerations on the CFD simulations are not present in the force results. Fig. 13 shows that in the attached flow case, the mean values of the CFD simulations and the single point vortex model lies within 20%, whilst the agreement of the mean tangential forces lies within 3%. It is observed that the variance around the mean value of the radial force is captured well with the point vortex model with Theodorsen's effect. If the correction is not included, the mean value remains constant, but the variance increases, as shown previously in Fig. 5. Therefore, we show that the effect of the wake, modelled through Theodorsen's function, is to reduce the peak to peak loading around the foil, rather than altering its mean loading.

6.4. Instantaneous radial loading on foil

To understand the instantaneous loading characteristics of the cyclorotor, in this Section, we compare the instantaneous radial force R of the attached ($T = 1.8$ s, $H = 0.253$ m) and vortical flow cases ($T = 2.4$ s, $H = 0.313$ m) computed with CFD. We analyse R because it is the force component that is responsible for the bending moments and stresses on the foil, and because it is the force component that showed the highest variance, with respect to the mean, in Fig. 13. We recall that $R_{av} = 300,000$ for the attached flow case, while $R_{av} = 250,000$ for the vortical flow case. Note that although the Reynolds number is slightly different between the two cases, any significant difference in the loading is due to the different flow physics rather than the effect of the Reynolds number.

We plot the instantaneous R during one full cycle T after $35T$ in the polar plot of Fig. 14. Results are shown for both attached and vortical flow cases. For comparison, we also present the average R computed with the point vortex model for the case of attached flow. We note that R is defined at the quarter chord position of the foil and that it is positive inwards pointing towards the central shaft. In the figure the azimuthal angle denotes the rotor position and the radial coordinate denotes R in Newtons.

Fig. 14 shows that the loading on the foil remains relatively constant for the case of attached flow. This is in agreement with the flow field observations presented in Fig. 10, in which the flow around the foil remains largely unaltered at $\theta = 0°, 90°, 180°$ and $270°$. The figure confirms that the average value of R predicted by the single point vortex model ($\overline{R}$ - blue dotted line) lies within 20% of the magnitude of R computed with CFD (black line).

In contrast, for the vortical flow case, R (red line) increases from $\theta = 0°$ to $\theta = 68°$ to a maximum value of about 80 N. Then, R

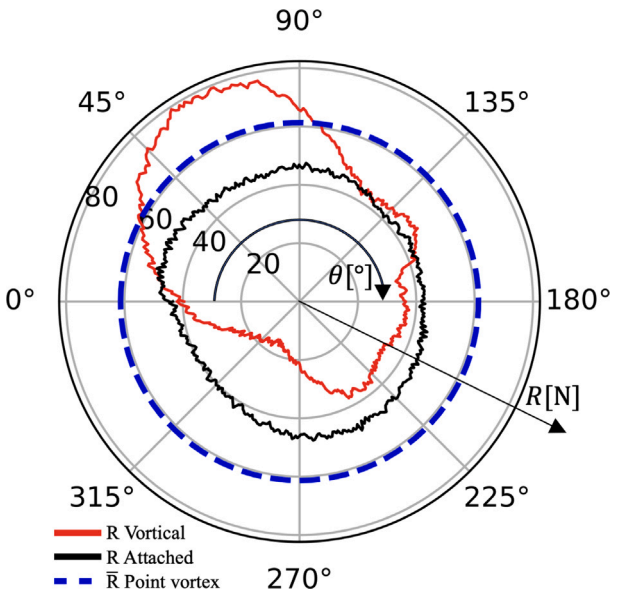

Fig. 14. Radial forces R for attached and vortical flow conditions computed from CFD and from analytical model for the case of attached flow, during one period of revolution t/T_p.

remains relatively constant until about $\theta = 80°$, after which R drops and stabilises at around 115° at approximately 40 N. Then, R remains stable at a value close to 40 N until 225°, after which it drops further to its lowest value of 18 N at approximately 300°. Lastly, R slowly recovers to a value of 40 N at 0° to start the cycle again.

Although we only have information from four azimuthal positions of the flow field around the foil, at $\theta = 0°$, $\theta = 90°$, $\theta = 180°$ and $\theta = 270°$, the trend in R can be explained through these flow field snapshots and the impulse of a vortex pair [27,53,55]. As evidenced in Fig. 10, a clear vortex pair is formed at $\theta = 90°$, whilst the pair is at its infant state at $\theta = 0°$. From the flow field observations, it can be observed that between $\theta = 0°$ and $\theta = 90°$, the circulation of the LEV and TEV grows, and that the convection velocity of the LEV is slower than the one of the TEV. Hence, both terms, circulation growth and advection velocity of the LEV explain the increase in R of the foil [27,53]. Then, the LEV is likely to reach the advection velocity of the TEV and it dissipates in the wake. This probably explains the initial drop in R. The flow is attached to the foil at $\theta = 180°$, and because the initial vortex pair has dissipated, it is likely that the stable value of R at about 40 N is due to attached flow over the range of $115° < \theta \leq 225°$. Lastly, at $\theta = 270°$, an LEV is present on the suction side of the foil, however, in this case the TEV has started to dissipate and is further downstream of the foil. Hence a vortex pair with cores of opposite and equal circulation is not formed. However, the presence of the LEV influences and reduces any bound circulation on the foil [53,56,57]. As such, the force decreases in the vicinity of this azimuthal angle. Lastly, the force recovers at $\theta = 0°$, as the new vortex pair starts to emerge. Hence, because of these large oscillations around the mean radial force, that occur typically in dynamic stall [24], it is structurally preferred to operate a cyclorotor in attached flow conditions to reduce likelihood of fatigue damage.

In the next Sections, we size a large scale cyclorotor in terms of optimum radius for power production, and optimum span to maintain the bending stress at the foil at the allowable stress level. We consider that the chord of the foil is equal to the radius of the rotor, as suggested in [17]. We use the point vortex and structural models developed in Sections 3 and 5. It is expected that the optimal chord length identified in [17], and the optimal radius for power performance, will steer the rotor to operate in attached flow conditions, close to stall, at maximum lift conditions. This is similar to what has been observed in tidal turbines that operate in optimal conditions, in which attached flow dominates and dynamic stall is not influential [25,58].

6.5. Operational and structural design at wave design conditions

In this section we focus on finding the optimal operational phase and structural parameters for a large scale rotor under regular waves. Specifically, we focus on the selection of a radius that optimises power extraction and of a span length that maintains the bending stresses at the allowable stress level.

We first illustrate a sample case assuming a monochromatic wave that represents the fundamental wave of the panchromatic spectrum at wave design conditions, i.e. T_p= 9 s and H_s= 1.2 m. We can then compute H and T, to be used in Eqs. (9) and (10), as $H = H_s/\sqrt{2}$ and $T = T_p$. The submergence of the rotor is defined as $z_0 = -1.5r - 0.5H_s$ and a foil span of 10 m is initially assumed. We plot the contour plots of the mean power output $\overline{P}$ and the maximum amplitude of the bending stresses σ_{qc}, in Fig. 15a and 15b, respectively. In both figures, ϕ is plotted on the horizontal axis over a range of 0° to 180°, whilst r is plotted on the vertical axis over a range of 1 to 12 m. The foil has a chord length equal to r. This is based on the findings of Siegel [17], who suggests optimal power capture when $c/r = 1$. The pitch angle of the foil is set to 0°.

Fig. 15a shows that for any r, the optimal phase ϕ_{opt} is $\phi = 90°$. This is because at this ϕ, the tangential component of the lift force acting on the foils is maximised. Any other ϕ results in a drop of the tangential force and therefore, of the mean output power. Noteworthy, when $\phi = 0°$ and $\phi = 180°$, i.e. when the rotor is rotating in phase with the wave, $\overline{P}$ drops below zero. The figure also shows that $\overline{P}$ grows with r until an optimal r value, after which $\overline{P}$ starts to drop again. It can be seen that the optimal operating condition is when r is optimal and $\phi = 90°$. For this particular case r_{opt} is 5.5 m, as shown in Fig. 15a. This is within 8% of r_{opt} found in previous wave cycloidal research [17]. We note, however, that larger wave design conditions were used in [17] to the ones used in this paper.

Fig. 15b shows a central band of high stresses at $\phi = 90°$. This band shows that σ_{qc} grows rapidly to a maximum of σ_{qc} = 15 MPa, at r = 3 m, and that it then decreases gradually to about σ_{qc} = 8 MPa. Note that even though the radial and bending moments on the foil grow with r, in this case, σ_{qc} decreases after it reaches its maximum value at r = 3 m. This is because I_{xx} also grows with the radius, but at a greater rate than the radial forces. Hence, the structural design of the cross section, specifically I_{xx}, determines the distribution of σ_{qc} with respect to r. Because Fig. 15b shows that $\sigma_{qc} \leq \sigma_a$ for any ϕ and any r, we utilise Fig. 15a to determine r_{opt} and ϕ_{opt}.

Once ϕ_{opt} and r_{opt} are determined, we can select the optimum span of the foil s_{opt}. The larger the span, the more power the cyclorotor can produce, however, the loads and the span cannot be infinitely large due to their impact on the bending stresses of the foils. In this work, we apply the condition that the maximum bending stresses $\sigma_{qc} \leq \sigma_a$. We recall, from Table 1, that for offshore steel σ_a = 117 MPa.

Fig. 16 shows σ_{qc} versus different foil spans. We present results for uniform loading. In the plot, σ_{qc} is plotted for r_{opt} = 5.5 m, r_{low} = 3 m and r_{high} = 10 m; where r_{low} and r_{high} define a range of radii, in which the bending stresses drop gradually from maximum to minimum values, as indicated in Fig. 15b. In Fig. 16, the black line shows σ_{qc} in the foil at r_{opt}, whilst the pink and blue line show σ_{qc} at r_{low} = 3 m and r_{high} = 10 m, respectively. Stresses for intermediate radii are plotted with dashed grey lines in steps of 1 m between r_{low} and r_{high}. The allowable stress level σ_a and the yield stress level σ_y are shown with horizontal green and red dotted lines, respectively.

The span of the rotor is given by the intersection of the r_{opt} curve (solid black line) and the σ_a curve (dotted green line). At this intersection point, a vertical line is drawn to determine the span of the rotor that will satisfy $\sigma_{qc} \leq \sigma_a$. Therefore, in Fig. 16, we find that for the same monochromatic wave, that we used in Fig. 15, $s_{opt}/r_{opt} \approx 5.5$. Different materials for the foils could yield different s/r ratios. We recall that in this work, we use offshore steel as construction material for the spar. In contrast, the s_{opt}/r_{opt} ratio of the Atargis cyclorotor is $s_{opt}/r_{opt} \approx 10$

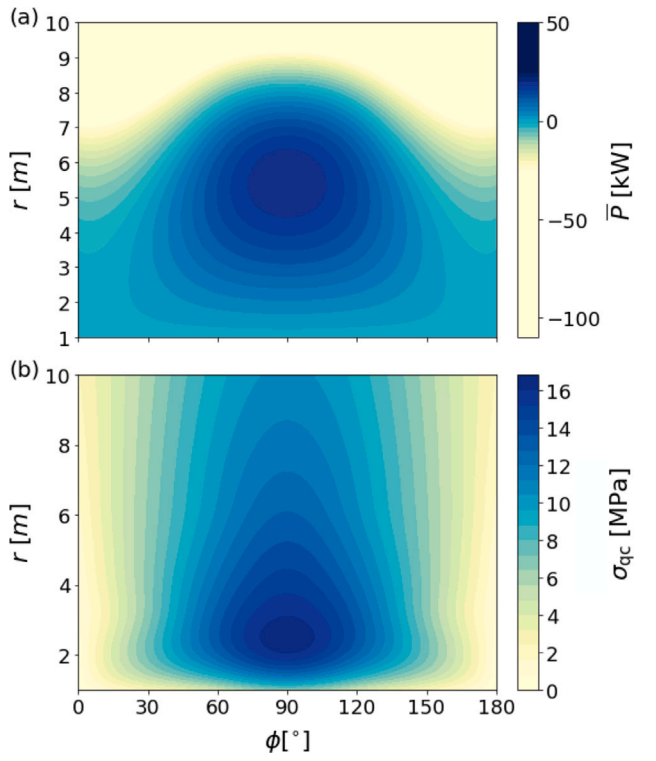

Fig. 15. (a) Mean output power $\overline{P}$ and (b) maximum amplitude of bending stresses σ_{qc} plotted as a function of ϕ and r for a monochromatic wave that represents the fundamental wave of the panchromatic wave spectrum at design sea state conditions ($H_s = 1.2$ m and $T_p = 9$ s), and assuming 10 m span.

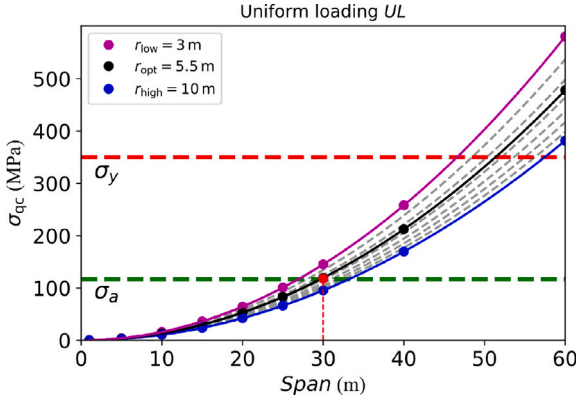

Fig. 16. Bending stresses (σ_{qc}) versus span (s) for different rotor radii. The blue, black and pink lines correspond to r_{high}, r_{opt} and r_{low}, respectively. The dotted grey lines correspond to intermediate radii. The green and red horizontal lines correspond to σ_a and σ_y, respectively. The red marker with the vertical dotted line show the selected span of the foil.

with foils made of composite material [2]. However, the methodology demonstrated here for sizing the rotor is independent of the material of the foil. In the next section, we explore the effect of different sea states in the s_{opt}/r_{opt} ratio. We note that although only results for uniform loading are presented, elliptical loading yields a reduction in s_{opt} of about 5%.

6.6. Sizing of rotor for different sea states

The previous sections showed that there is an optimum radius r_{opt} and optimum phase ϕ_{opt} at which the mean power output is maximised. We also showed that assuming r_{opt} and ϕ_{opt}, the optimum span of the rotor s_{opt} can be found, so that the σ_{qc} at the fixed end of the foil remain at the allowable stress level σ_a. In this section, we find the optimum radius r_{opt} for different wave conditions assuming operation at ϕ_{opt}. We then find s_{opt} for the same range of wave conditions.

We use H_s and T_p to present our results. Note, however, that H_s and T_p, represent the fundamental wave in the panchromatic spectrum only. We recall that, $H_s = \sqrt{2}H$ and $T_p = T$, where H and T are used as inputs in Eqs. (9) and (10). In agreement with Section 6.5, the submergence of the rotor is defined as $z_0 = -1.5r - 0.5H_s$. A constant span of 30 m is assumed initially, as suggested in the results of Fig. 16. Results for r_{opt} are shown in Fig. 17a. The horizontal axis shows T_p over a range of 6 to 16 s and the vertical axis H_s over a range of 1 to 5 m. The figure shows that r_{opt} grows with T_p and H_s.

Even though r_{opt} changes with T_p and H_s, as shown in Fig. 17a, it is expected that a large scale rotor will have a fixed radius. As such, r_{opt} is likely to be determined by the sea state condition with the highest probability of occurrence in a given location. Recalling that in Fig. 2, the sea state with highest occurrence are those with $H_s \leq 2$ m and T_p between 6s and 12 s, it is envisioned that for this particular site, the value of r_{opt} would be between 4 to 6 m. This is agreement for example with the cycloidal wave rotor designed by Atargis corporation [2], which has been sized with a radius of 6 m.

Secondly, we find s_{opt} for the same range of wave conditions tested in Fig. 17a. We note that we consider a chord length equal to r_{opt}, as proposed by Siegel [1,2]. Hence, we denote this chord length as the optimum chord length c_{opt}. Results for s_{opt} are shown in Fig. 17b through the optimum aspect ratio ($\mathcal{AR}_{opt} = s_{opt}/c_{opt}$). It can be seen that $\mathcal{AR}_{opt}$ is relatively independent of T_p, and decreases with increasing H_s. The largest $\mathcal{AR}_{opt}$ values occur towards the bottom part of Fig. 17b. In fact, because the probability of sea states is higher towards this bottom region of the figure, it is expected that a large scale rotor is sized to have an $\mathcal{AR}_{opt}$ between 6 to 8. This is not distant from the Atargis cyclorotor, which is sized with $\mathcal{AR}_{opt} = 10$ [2]. Note, however, that different values of $\mathcal{AR}_{opt}$ can be attributed to material selection, design of hydrofoil cross section and specification of σ_a. Here, we recall that we use offshore steel and $\sigma_a = 117$ MPa, as indicated in Table 1. In the results of Fig. 17b, we assume uniform loading, although results for elliptical loading yielded lower $\mathcal{AR}_{opt}$ values by approximately 5%.

Finally, to assess the power capabilities of the single foil rotor and the stress level at the fixed end of the foils after sizing r_{opt} and s_{opt}, we compute the average power ($\overline{P}$) and the bending stresses (σ_{qc}) in Fig. 18a and 18b, respectively. We use the same H_s and T_p combinations that we used in Fig. 17a and 17b.

We observe in Fig. 18a that $\overline{P}$ increases with H_s and T_p, whilst the stress level in Fig. 18b remains within ± 1% of 117 MPa. The increase in $\overline{P}$ with wave height is in agreement with previous power matrices of wave cyclorotors [2,11]. We note however, that different to these studies, the power matrix presented here shows the maximum $\overline{P}$ at the top right corner of Fig. 18a and that power generation is possible also at very low H_s and T_p. This is because the power matrix of this work considers optimum power production through r_{opt}, whilst at the same time, structural reliability by maintaining the stress level at the allowable threshold, as shown in Fig. 18b.

The results presented in this section highlight two important aspects in wave cyclorotor design that have not been addressed previously in the literature. Firstly, that through appropriate r and s sizing or that through variable r and s, it is theoretically possible to generate power with wave cyclorotors even at low H_s and low T_p. This increases the range of locations where wave cycloidal rotors could be deployed. Secondly, that if a designer opts to increase the radius of the rotor, the span of the foil needs to be reduced to remain structurally resilient. However, this also means that a large span rotor could be reinforced with intermediate supports to reduce the free hanging parts of the foil. As such, our results provide guidelines for power production and resilient structural design at the significant wave conditions of a site. In addition to appropriate sizing, several control techniques,

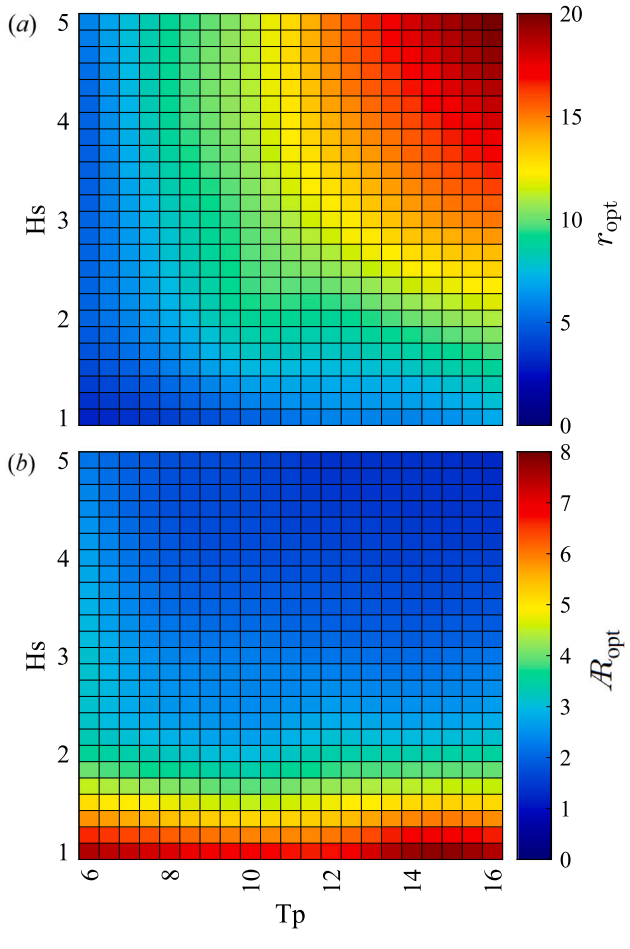

Fig. 17. (a) Optimum radius r_{opt} and (b) $\mathcal{AR}_{opt}$ for different wave conditions for a single foil cyclorotor.

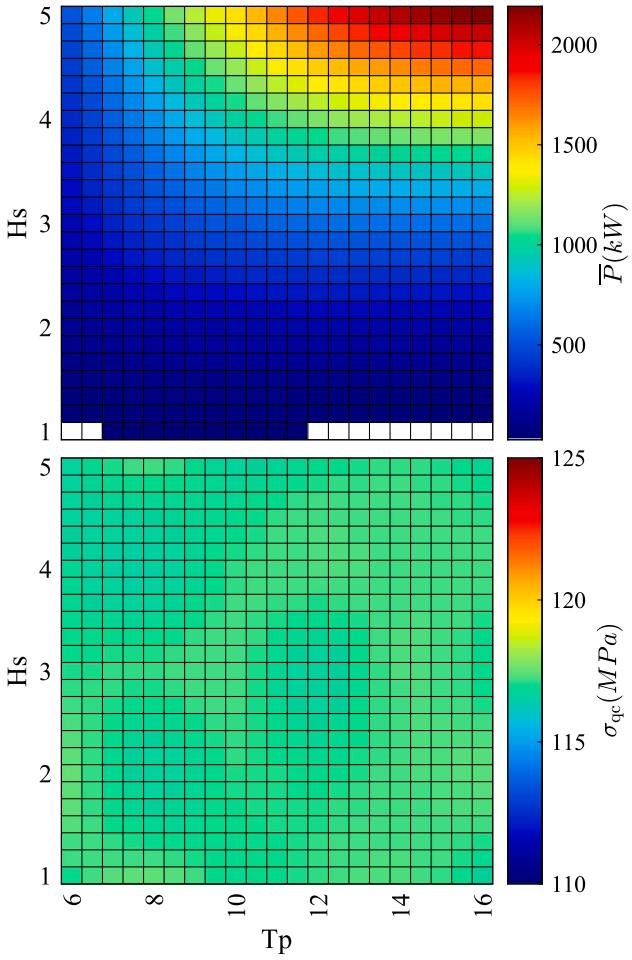

Fig. 18. (a) Power matrix in kW and (b) stress level at fixed end of the foils with uniform loading in MPa for rotor at ϕ_{opt}, r_{opt} and $\mathcal{AR}_{opt}$.

such as variable rotational velocity [59] and fatigue damage mitigation strategies, such as passively [28,60] or actively pitching foils [61], could help in increasing power extraction, whilst reducing the loads on the foil and cyclorotor.

7. Two foil rotor considerations

Although the purpose of this paper is to advance the understanding of the hydrodynamics and structural design parameters of a single foil wave cycloidal rotor subject to regular waves, it is important to consider some relevant aspects of two foil wave cycloidal rotors, which have been studied in several recent studies [2,17,62,63].

Firstly, we reproduce the power matrix shown in Fig. 18a, by considering a rotor with two foils. We follow the model proposed in Ermakov and Ringwood [18], but different to their model, we define the position of foil 1 at $\theta = 0°$ as it is defined in this paper in Fig. 3, and the position of foil two at $\theta = 180°$.

Results are shown in Fig. 19, as the ratio $\overline{P}_2/\overline{P}$, where $\overline{P}_2$ is the average power produced with a two foil wave cycloidal rotor. We can observe that $\overline{P}_2/\overline{P}$ ranges between 1.8–2.1, throughout the power matrix. Hence, two foil rotors produce more power output than the single foil rotor studied in this paper, an also, have a redundancy element by including two, rather than one foil.

Secondly, we note that two or multiple foil rotor, might attenuate the instantaneous oscillations in power, due to the complementary effect of the foils operating at different angle. Similar to multibladed cross flow turbines [23]. However, this topic is subject of further studies for wave cycloidal rotors.

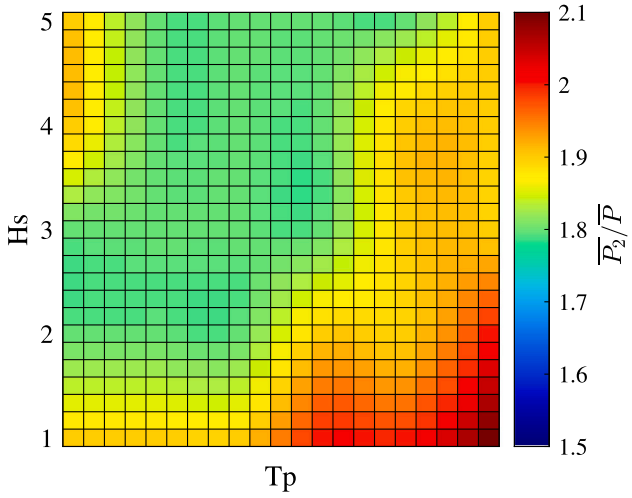

Fig. 19. Power matrix of ratio $\overline{P}_2/\overline{P}$, where $\overline{P}_2$ refers to the mean power output of a two foil wave cycloidal rotor.

8. Conclusions

In this paper, the hydrodynamics and the structural design of a single foil wave cycloidal rotor in regular waves have been studied.

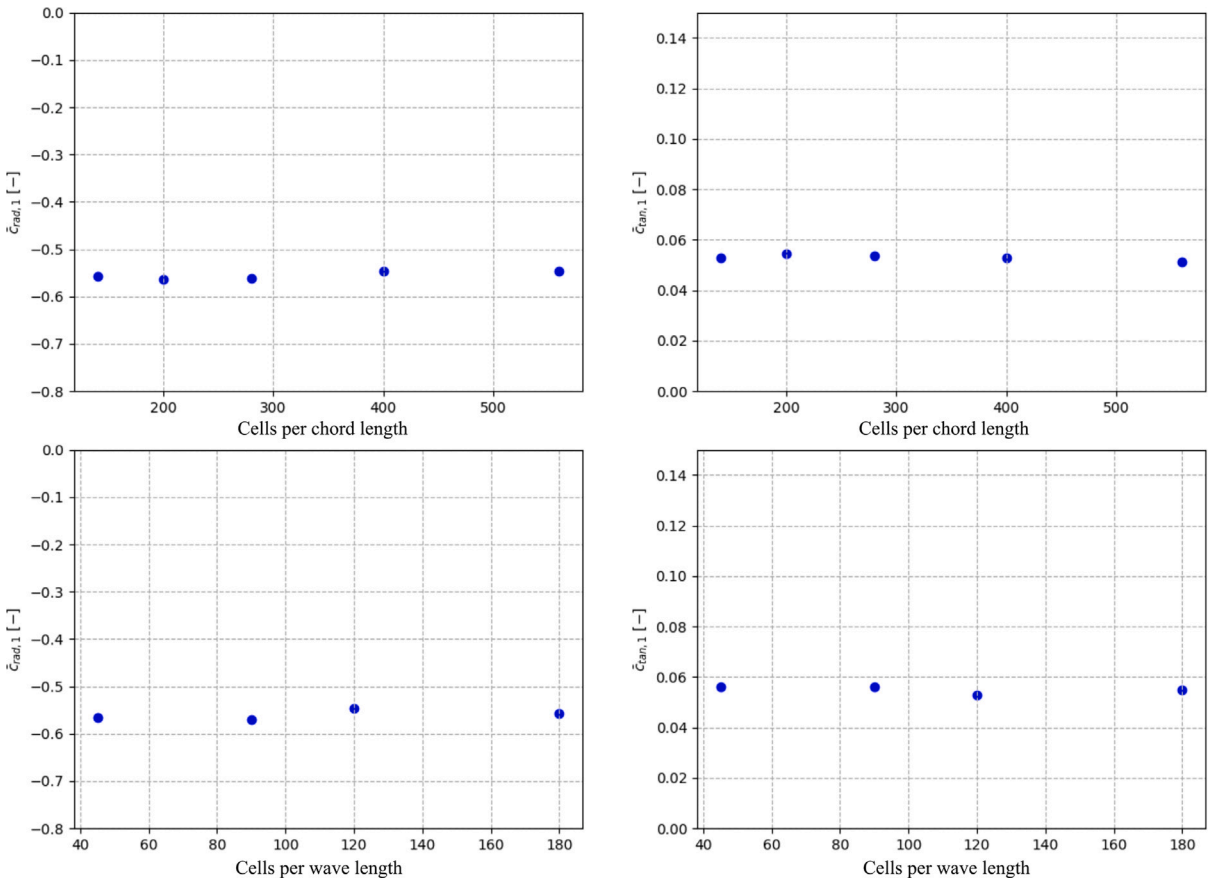

Fig. 20. Grid and time resolution study for 2D simulations of single foil rotor in regular waves.

We do this by developing a potential flow model coupled to a structural model to design single foil cyclorotors in an efficient manner. The potential flow model considers unsteady wake effects through Theodorsen's theory.

To understand better the flow physics of the wave cycloidal rotor and the limitations of the potential flow model, we analysed the flow field around a single foil rotor with the aid of two dimensional RANS simulations. A laboratory scale type of rotor was studied. Two flow conditions were analysed, attached and vortical flow conditions. It was found that attached flow conditions are desirable to minimise radial loading fluctuations, and therefore reducing the potential due to fatigue damage. In contrast, vortical flows yield large radial amplitude oscillations, which are undesirable for the structural reliability of the rotor.

We demonstrate that CFD simulations yield realistic results by comparing the mean force and tangential estimates to two dimensional experimental data of a single foil rotor. Then, by comparing the CFD with the potential flow model results, we found that under attached flow conditions, the potential flow model yields reasonable accuracy, within 20%–25% of the mean radial force. In contrast, the radial force is estimated successfully, only when the rotor operates close to stall, i.e. at maximum lift operating conditions. However, because the optimal hydrodynamic and structural operation of the rotor is expected to occur under attached flow conditions and close to stall, at maximum lift conditions, the analytical model is considered a useful tool and is utilised to find the optimum radius for power production, and the span that allows the foil of the cyclorotor to remain at the allowable stress level.

By assuming monochromatic waves that represent the fundamental wave of the panchromatic spectrum, we carry out the structural analysis of the cyclorotor. We find that because the optimal structural aspect ratio and optimal radius of operation change with different wave conditions, the dimensions for a fixed span fixed radius rotor are likely to be determined by the sea state with highest probability of occurrence. Hence, we find that for $H_s = 1.2$ m and $T_p = 9$ s, the optimum radius is $r_{\text{opt}} = 5.5$ m, with an optimal aspect ratio $\mathcal{AR}$ between 6 to 8. We note, however, that the $\mathcal{AR}$ values are dependent on the type of material and cross section considered to design the hydrofoil of the cyclorotor.

The novelty of the results presented in this paper include, for the first time in the literature of wave cycloidal rotors, a detailed flow field characterisation of a single foil rotor. We show, for the first time, under what flow conditions a single point vortex potential flow model can be used to estimate the forces of the rotor subject to regular waves. These findings contribute and pave the way to further advance the research and development of cycloidal rotors for wave energy conversion.

CRediT authorship contribution statement

Abel Arredondo-Galeana: Writing – original draft, Conceptualization, Methodology, Formal analysis, Investigation, Data processing. **Gerrit Olbert:** Writing – review & editing, Conceptualization, CFD simulations. **Weichao Shi:** Writing – review & editing, Conceptualization, Supervision, Funding acquisition. **Feargal Brennan:** Writing – review & editing, Conceptualization, Supervision, Funding acquisition.

Declaration of competing interest

The authors declare that they have no known competing financial interests or personal relationships that could have appeared to influence the work reported in this paper.

Acknowledgements

The authors would like to thank all the members of the LiftWEC consortium for the fruitful discussions and inputs that made this work possible. We would also like to thank the European Union's Horizon 2020 Research and Innovation Programme under Grant Agreement No 851885. Lastly, we would like to thank the two anonymous reviewers that helped greatly in improving the quality of this manuscript.

Appendix. CFD grid independence study

Fig. 20 shows the results of a grid resolution study during which different levels of free surface and foil surface resolution were applied while simulating the interaction of a single foil rotor and a monochromatic wave. The results present the mean radial and tangential force coefficients obtained for each setting. During the foil surface resolution study, 120 cells per wave length were used to resolve the free surface. During the free surface resolution study, 400 cells per chord length were used to resolve the foil surface. For each stage of horizontal grid refinement, vertical resolution of the free surface was adjusted accordingly. The time step size was kept constant through all simulations, with Δt corresponding to $\Delta\theta = \frac{\sqrt{2}}{2}^{\circ}$, which was found to provide CFL < 0.25 in the vicinity of the free surface in all simulations.

The resulting forces are evaluated in terms of mean radial and tangential forces at quarter chord position. After 3–4 wave cycles, the forces were observed to adopt a nearly periodic behaviour, with differences in oscillation mostly due to a wake memory effect, i.e. the foil passing through its own wake region. The mean forces are obtained by taking the mean values between the 4th and the 8th wave cycle (see Eqs. (31), (32)).

$$\bar{F}_{rad} = \frac{1}{4T}\int_{t=4T}^{t=8T} F_{rad,x/c=\frac{1}{4}}\,dt \tag{31}$$

$$\bar{c}_{rad} = \frac{\bar{F}_{rad}}{0.5\rho(\omega r)^2 c} \tag{32}$$

In both studies, the mean radial force coefficient at quarter chord position $\bar{c}_{rad}$ shows only small variations, with absolute values ranging between $\bar{c}_{rad} = 0.54$ and $\bar{c}_{rad} = 0.56$. As may be expected, the results do not show a monotoneous convergence behaviour. This is the result of the described memory effect, with slight variations in inflow direction leading to variations in resulting wake field, which again leads to a variation of inflow conditions.

The tangential force coefficient shows similarly small variations, with mean values varying between $\bar{c}_{tan} = 0.053$ and $\bar{c}_{tan} = 0.057$. The relative variability is slightly higher than for the radial force. Nevertheless, consistency of mean forces over all resolution settings still appears high. A resolution of 200 cells per chord length and 90 cells per wave length was subsequently applied to the CFD based results presented in this manuscript.

References

[1] S. Siegel, T. Jeans, T. McLaughlin, Deep ocean wave energy conversion using a cycloidal turbine, Appl. Ocean Res. 33 (2) (2011) 110–119, http://dx.doi.org/10.1016/j.apor.2011.01.004.

[2] S.G. Siegel, Numerical benchmarking study of a cycloidal wave energy converter, Renew. Energy 134 (2019) 390–405, http://dx.doi.org/10.1016/j.renene.2018.11.041.

[3] A. Arredondo-Galeana, W. Shi, G. Olbert, M. Scharf, A. Ermakov, J. Ringwood, F. Brennan, A methodology for the structural design of LiftWEC: A wave-bladed cyclorotor, in: Proceedings of the 14th European Wave and Tidal Energy Conference, 2021.

[4] A. Ermakov, J.V. Ringwood, Rotors for wave energy conversion—Practice and possibilities, IET Renew. Power Gener. 15 (2021) 3091–3108, http://dx.doi.org/10.1049/rpg2.12192.

[5] G. Olbert, M. Scharf, S. Felten, M. Abdel-Maksoud", Comparison of RANS and potential flow theory based simulations of a cyclorotor type wave energy converter in regular waves, in: D. Greaves (Ed.), Proceedings of the Fourteenth European Wave and Tidal Energy Conference, EWTEC, University of Plymouth, UK, 2021, ISSN: 2309-1983.

[6] Y. Cao, A. Liu, X. Yu, Z. Liu, X. Tang, S. Wang, Experimental tests and CFD simulations of a horizontal wave flow turbine under the joint waves and currents, Ocean Eng. 237 (2021) 109480, http://dx.doi.org/10.1016/j.oceaneng.2021.109480.

[7] A. Hermans, E. Van Sabben, J. Pinkster, A device to extract energy from water waves, Appl. Ocean Res. 12 (4) (1990) 175–179, http://dx.doi.org/10.1016/S0141-1187(05)80024-0.

[8] J. Chaplin, C. Retzler, Predictions of the hydrodynamic performance of the wave rotor wave energy device, Appl. Ocean Res. 17 (6) (1995) 343–347, http://dx.doi.org/10.1016/S0141-1187(96)00017-X.

[9] P. Lamont-Kane, M. Folley, C. Frost, T. Whittaker, Preliminary investigations into the hydrodynamic performance of lift-based wave energy converters, in: Proceedings of the 14th European Wave and Tidal Energy Conference, 2021.

[10] M. Folley, P. Lamont-Kane, Optimum wave regime for lift-based wave energy converters, in: Proceedings of the 14th European Wave and Tidal Energy Conference, 2021.

[11] A. Ermakov, J.V. Ringwood, A control-orientated analytical model for a cyclorotor wave energy device with N hydrofoils, J. Ocean Eng. Mar. Energy 7 (2) (2021) 201–210.

[12] J.P. Sierra, A. White, C. Mösso, M. Mestres, Assessment of the intra-annual and inter-annual variability of the wave energy resource in the Bay of Biscay (France), Energy 141 (2017) 853–868, http://dx.doi.org/10.1016/j.energy.2017.09.112, URL http://www.sciencedirect.com/science/article/pii/S0360544217316328.

[13] M. Accensi, C. Maisondieu, Homere. Ifremer - laboratoire comportement des structures en mer, 2015, http://dx.doi.org/10.12770/cf47e08d-1455-4254-955e-d66225c9dc90.

[14] A.M. Cornett, A global wave energy resource assessment, in: Proceedings of the Eighteenth International Offshore and Polar Engineering Conference, 2008.

[15] T. Burton, N. Jenkings, Sharpe, Wind Energy Handbook, second ed., Wiley, 2011.

[16] J.V. Wehausen, E.V. Laitone, Surface waves, in: C. Truesdell (Ed.), Fluid Dynamics / Strömungsmechanik, Springer Berlin Heidelberg, Berlin, Heidelberg, 1960, pp. 446–778, http://dx.doi.org/10.1007/978-3-642-45944-3_6.

[17] S. Siegel, Wave climate scatter performance of a cycloidal wave energy converter, Appl. Ocean Res. 48 (2014) 331–343, http://dx.doi.org/10.1016/j.apor.2014.10.008, URL https://www.sciencedirect.com/science/article/pii/S0141118714001023.

[18] A. Ermakov, J.V. Ringwood, Development of an analytical model for a cyclorotor wave energy device, in: Proceedings of the 14th European Wave and Tidal Energy Conference, 2021.

[19] G.Z. McGowan, K. Granlund, M.V. Ol, A. Gopalarathnam, J.R. Edwards, Investigations of lift-based pitch-plunge equivalence for airfoils at low Reynolds numbers, AIAA J. 49 (7) (2011) 1511–1524, http://dx.doi.org/10.2514/1.J050924.

[20] G.B. Airy, Tides and Waves, (192) Encyc. Metro., 1985.

[21] M. McCormick, Ocean Wave Energy Conversion, Dover edition, Dover Publications Inc, 2013.

[22] R.E. Sheldahl, P.C. Klimas, Aerodynamic Characteristics of Seven Symmetrical Airfoil Sections Through 180-Degree Angle of Attack for Use in Aerodynamic Analysis of Vertical Axis Wind Turbines, Sandia National Laboratories, 1981, http://dx.doi.org/10.2172/6548367.

[23] A. Arredondo-Galeana, F. Brennan, Floating offshore vertical axis wind turbines: Opportunities, challenges and way forward, Energies 14 (23) (2021) http://dx.doi.org/10.3390/en14238000.

[24] S. Le Fouest, K. Mulleners, The dynamic stall dilemma for vertical-axis wind turbines, Renew. Energy 198 (2022) 505–520, http://dx.doi.org/10.1016/j.renene.2022.07.071.

[25] G.T. Scarlett, B. Sellar, T. van den Bremer, I.M. Viola, Unsteady hydrodynamics of a full-scale tidal turbine operating in large wave conditions, Renew. Energy 143 (2019) 199–213, http://dx.doi.org/10.1016/j.renene.2019.04.123.

[26] J.G. Leishman, Principles of Helicopter Aerodynamicsr, Cambridge University Press, 2002.

[27] S. Ōtomo, S. Henne, K. Mulleners, K. Ramesh, I.M. Viola, Unsteady lift on a high-amplitude pitching aerofoil, Exp. Fluids 62 (1) (2020) 6, http://dx.doi.org/10.1007/s00348-020-03095-2.

[28] A. Arredondo-Galeana, A.M. Young, A.S. Smyth, I.M. Viola, Unsteady load mitigation through a passive trailing-edge flap, J. Fluids Struct. 106 (2021) 103352, http://dx.doi.org/10.1016/j.jfluidstructs.2021.103352.

[29] C. Windt, J. Davidson, J.V. Ringwood, High-fidelity numerical modelling of ocean wave energy systems: A review of computational fluid dynamics-based numerical wave tanks, Renew. Sustain. Energy Rev. 93 (June) (2018) 610–630, http://dx.doi.org/10.1016/j.rser.2018.05.020.

[30] G. Olbert, M. Abdel-Maksoud, High-fidelity modelling of lift-based wave energy converters in a numerical wave tank [manuscript submitted for publication] (Ph.D. thesis), Fluid Dynamics and Ship Theory, Hamburg University of Technology, 2022.

[31] F.R. Menter, Two-equation eddy-viscosity turbulence models for engineering applications, AIAA J. 32 (1994) 1598–1605.

[32] B.E. Larsen, D.R. Fuhrman, On the over-production of turbulence beneath surface waves in Reynolds-averaged Navier-Stokes models, J. Fluid Mech. 853 (2018) 419–460, http://dx.doi.org/10.1017/jfm.2018.577.

[33] P. Durbin, On the k-ϵ stagnation point anomaly, Int. J. Heat Fluid Flow (17) (1996) 89–90, http://dx.doi.org/10.1016/0142-727X(95)00073-Y.
[34] R. Kumar, H. Shin, Thrust prediction of an active flapping foil in waves using CFD, J. Mar. Sci. Eng. 7 (11) (2019) 396, http://dx.doi.org/10.3390/JMSE7110396, https://www.mdpi.com/2077-1312/7/11/396.
[35] S. Zanforlin, F. Buzzi, M. Francesconi, Performance analysis of hydrofoil shaped and bi-directional diffusers for cross flow tidal turbines in single and double-rotor configurations, Energies 12 (2) (2019) 272, http://dx.doi.org/10.3390/EN12020272, https://www.mdpi.com/1996-1073/12/2/272.
[36] H.J.A. Bird, K. Ramesh, S. Ōtomo, I. Maria Viola, Usefulness of inviscid linear unsteady lifting-line theory for viscous large-amplitude problems, AIAA J. 60 (2) (2022) 598–609, http://dx.doi.org/10.2514/1.J060808.
[37] P. Marsh, D. Ranmuthugala, I. Penesis, G. Thomas, Three-dimensional numerical simulations of straight-bladed vertical axis tidal turbines investigating power output, torque ripple and mounting forces, Renew. Energy 83 (2015) 67–77, http://dx.doi.org/10.1016/j.renene.2015.04.014.
[38] S.C. Heavey, S.B. Leen, P.J. McGarry, An efficient computational framework for hydrofoil characterisation and tidal turbine design, Ocean Eng. 171 (December 2017) (2019) 93–107, http://dx.doi.org/10.1016/j.oceaneng.2018.10.032.
[39] T. Xing, K.I. Matveev, M.P. Wheeler, Numerical study of high-lift hydrofoil near free surface at moderate Froude number, J. Hydrodyn. 32 (1) (2020) 44–53, http://dx.doi.org/10.1007/s42241-019-0095-0.
[40] C.W. Hirt, B.D. Nichols, Volume of fluid (VOF) method for the dynamics of free boundaries, J. Comput. Phys. (1981) http://dx.doi.org/10.1016/0021-9991(81)90145-5.
[41] S. Rapuc, P. Crepier, F. Jaouen, T. Bunnik, P. Regnier, Towards guidelines for consistent wave propagation in CFD simulations, in: Technology and Science for the Ships of the Future - Proceedings of NAV 2018: 19th International Conference on Ship and Maritime Research, 2020, pp. 515–524, http://dx.doi.org/10.3233/978-1-61499-870-9-515.
[42] R. Meakin, Composite overset structured grids, in: Handbook of Grid Generation, CRC Press, 1998, http://dx.doi.org/10.1201/9781420050349.CH11.
[43] J.D. Fenton, A fifth-order stokes theory for steady waves, J. Waterway Port Coast. Ocean Eng. 111 (2) (1985) 216–234, http://dx.doi.org/10.1061/(ASCE)0733-950X(1985)111:2(216).
[44] R. Perić, M. Abdel-Maksoud, Reliable damping of free-surface waves in numerical simulations, Ship Technol. Res. 63 (1) (2016) 1–13, http://dx.doi.org/10.1080/09377255.2015.1119921, arXiv:1505.04087.
[45] F. Ursell, R.G. Dean, Y.S. Yu, Forced small-amplitude water waves: a comparison of theory and experiment, J. Fluid Mech. 7 (1) (1960) 33–52, http://dx.doi.org/10.1017/S0022112060000037.
[46] S. Yagmur, F. Kose, Numerical evolution of unsteady wake characteristics of H-type Darrieus Hydrokinetic Turbine for a hydro farm arrangement, Appl. Ocean Res. 110 (January) (2021) 102582, http://dx.doi.org/10.1016/j.apor.2021.102582.
[47] F. Brennan, I. Tavares, Fatigue design of offshore steel mono-pile wind substructures, in: Proceedings of the Institution of Civil Engineers Energy, Volume 167 Issue EN4, 2014, http://dx.doi.org/10.1680/ener.14.00005.
[48] S. Gudmundsson, General Aviation Aircraft Desigh. Applied Methods and Procedures, first ed., Butterworth-Heinemann, 2014.
[49] S.F. Hoerner, Fluid-Dynamic Lift: Practical Information on Aerodynamic and Hydrodynamic Lift, second ed., Hoerner Fluid Dynamics, 1975.
[50] J.D. Taylor, D.F. Hunsaker, Minimum induced drag for tapered wings including structural constraints, J. Aircr. 57 (4) (2020) 782–786.
[51] C. Simão Ferreira, G. van Kuik, G. van Bussel, F. Scarano, Visualization by PIV of dynamic stall on a vertical axis wind turbine, Exp. Fluids 46 (1) (2009) 97–108, http://dx.doi.org/10.1007/s00348-008-0543-z.
[52] P. Bot, Force variations related to flow pattern changes around a high-camber thin wing, AIAA J. 58 (5) (2020) 1906–1912, http://dx.doi.org/10.2514/1.J058443.
[53] I.M. Viola, A. Arredondo-Galeana, G. Pisetta, The force generation mechanism of lifting surfaces with flow separation, Ocean Eng. 239 (2021) 109749, http://dx.doi.org/10.1016/j.oceaneng.2021.109749.
[54] F. Thiebaut, G.S. Payne, Deliverable 4.2 - Report on physical modelling of 2D LiftWEC concepts, Technical Report, LiftWEC project, 2021, URL https://liftwec.com/wp-content/uploads/2021/11/LW-D04-04-1x0-Report-on-physical-modelling-of-2D-LiftWEC-concepts.pdf.
[55] H. Babinsky, R.J. Stevens, A.R. Jones, L.P. Bernal, M.V. Ol, Low order modelling of lift forces for unsteady pitching and surging wings, in: 54th AIAA Aerospace Sciences Meeting, 2016, http://dx.doi.org/10.2514/6.2016-0290.
[56] A. Arredondo-Galeana, I.M. Viola, The leading-edge vortex of yacht sails, Ocean Eng. 159 (2018) 552–562, http://dx.doi.org/10.1016/j.oceaneng.2018.02.029.
[57] A. Arredondo-Galeana, A study of the vortex flows of downwind sails, (Ph.D. thesis), 2019.
[58] P.W. Galloway, L.E. Myers, A.S. Bahaj, Quantifying wave and yaw effects on a scale tidal stream turbine, Renew. Energy 63 (2014) 297–307, http://dx.doi.org/10.1016/j.renene.2013.09.030.
[59] A. Ermakov, A. Marie, J.V. Ringwood, Optimal control of pitch and rotational velocity for a cyclorotor wave energy device, IEEE Trans. Sustain. Energy (2022) http://dx.doi.org/10.1109/TSTE.2022.3168508.
[60] A. Arredondo-Galeana, A. Ermakov, W. Shi, J.V. Ringwood, F. Brennan, Control strategies for power enhancement and fatigue damage mitigation of wave cycloidal rotors, http://dx.doi.org/10.2139/ssrn.4346306.
[61] N. Scharmann, Ocean energy conversion systems: The wave hydro-mechanical rotary energy converter, (Ph.D. thesis), Institute for Fluid Dynamics and Ship Theory, Hamburg, Germany, 2014.
[62] A. Ermakov, A. Marie, J.V. Ringwood, Some fundamental results for cyclorotor wave energy converters for optimum power capture, IEEE Trans. Sustain. Energy (2022) http://dx.doi.org/10.1109/TSTE.2022.3171711.
[63] J.V. Ringwood, A. Ermakov, Energy-maximising control philosophy for a cyclorotor wave energy device, in: 41st International Conference on Ocean, Offshore & Arctic Engineering (OMAE), Hamburg, American Society of Mechanical Engineers, 2022.

Abel Arredondo-Gaelana is a Research Associate at the Department of Naval, Marine and Ocean Engineering at the University of Strathclyde.

Gerrit Olbert is a Research Assistant at the Institute for Fluid Dynamics and Ship Theory, Hamburg University of Technology.

Weichao Shi is a Lecturer at the Department of Naval, Marine and Ocean Engineering at the University of Strathclyde.

Feargal Brennan is Head of the Department of Naval, Marine and Ocean Engineering at the University of Strathclyde.